TRAINING COURSE ON THE MANAGEMENT AND APPLICATION OF METEOROLOGICAL SATELLITE DATA

Sao Jose dos Campos

Sao Paulo, Brazil

TECHNICAL BACKGROUND FOR LECTURES AND EXERCISES ON QUANTITATIVE PROCESSING

William L. Smith
NOAA/NESDIS Development Laboratory
University of Wisconsin
1225 West Dayton Street
Madison, Wisconsin 53706

November 1983

Table of Contents

1.0 Radiative Transfer Processes Utilized for Satellite Remote Sensing

1.1 Remote Sensing: Definition

Remote sensing can be defined as the observation of a target by a device separated from it by some distance (e.g., eyes and ears are remote sensors via sensing reflected radiation and acoustic waves). Remote sensing with satellites is restricted to the use of radiation since it is a process whereby energy is transferred across space without the necessity of a material medium (contrasted with conduction, convection or advection). In remote sensing we make use of the effects of temperature and absorbing constituents (e.g., water vapor) on the spectral distribution of the sun's incoming or the earth's outgoing radiation.

1.2 Blackbody Radiation

The blackbody spectrum is the distribution of emitted energy in the absence of an atmosphere and for a "perfect emitter" is given by Planck's Law. The monochromatic intensity of radiation (B_λ) from blackbodies (perfect absorber and emitter of radiation) is given by the following expression

$$B_\lambda = \frac{C_1 \lambda^{-5}}{e^{C_2/\lambda T} - 1} \tag{1.1}$$

where C_1 and C_2 are universal constants, λ is wavelength, and T is temperature. The wavelength of maximum emission is obtained setting $\partial B_\lambda / \partial \lambda = 0$ yielding Wien's displacement law;

$$\lambda_m = \frac{2897 \ \mu m^\circ K}{T^\circ K} \tag{1.2}$$

For the sun (T=6000°K), $\lambda_m \tilde{\sim} 0.5$ μm, which is near the center of the visible region of the spectrum, whereas for earth (T=245°K), $\lambda_m \tilde{\sim} 11$ μm, which is in the infrared. Thus, the spectral distribution of incoming solar radiation is quite different from that of outgoing terrestrial radiation (fig. 1.1).

1.3 Basic Units

Radiant energy is observed to have a wave form and to travel in all directions away from a source with the speed of light c (=3 x 10^{10} cm/sec). The wavelength and frequency, f, are related by $\lambda=c/f$. The wavenumber, ν, is given by $1/\lambda$. For example, a 10 μm (10^{-3} cm) wavelength is equivalent to a wavenumber of 1000 cm^{-1}. Conversion of wavelength and frequency units is as follows:

$$1m = 10^2 \text{ cm} = 10^6 \text{ μm} = 10^{10} \text{ Å (Angstroms)}$$

and

$$1 \text{ cm}^{-1} = 3 \times 10^{10} \text{ Hz} = 30 \text{ GHz}.$$

1.4 The Spectrum

Table 1.1 shows the approximate ranges for the wavelengths and frequencies of the various kinds of radiation in the electromagnetic spectrum that can be used for remote sensing.

1.5 Absorbing Regions of the Spectrum

All of the regions of the spectrum described in Table 1.1 have important absorbing intervals (bands) or lines that are used in remote sensing. These are summarized in Table 1.2 for the more important atmospheric absorbers.

1.6 Asymptotic Relations

In units of wavenumber the Planck radiance is given by

$$B(\nu,T) = \frac{C_1 \nu^3}{e^{C_2 \nu/T}-1} \tag{1.3}$$

where T is the radiating temperature (usually called brightness temperature), $C_1=1.2\text{x}10^{-9}$ mw cm^2 str^{-1} and $C_2=1.44$ cm deg. For large ν (small wavelength), $e^{C_1 \nu/T}$ is much greater than unity so that

$$B(\nu,T) = C_1 \nu^3 e^{-C_2 \nu/T} = K(\nu) e^{-C_2 \nu/T} \tag{1.4}$$

such that radiance is highly non-linear with temperature (Wien's radiation law). For small ν (large wavelength) one can use the approximation that $e^{C_2\nu/T} = 1 + C_2\nu/T$ so that

$$B(\nu,T) = \frac{C_1\nu^3}{1 + \frac{C_2\nu}{T} - 1} = \frac{C_1}{C_2}\nu^2 T = K(\nu)T \qquad (1.5)$$

(Rayleigh-Jeans radiation law) where $K(\nu) = 8.33 \times 10^{-10} \nu^2$ mw cm str^{-1} deg^{-1}. The linear approximation (1.5) is valid to better than 1% for wavelengths greater than 320 μm.

1.7 Emissivity, Transmissivity, Reflectivity, Absorptivity

Real bodies are generally non-black (i.e., they do not emit according to Planck's law). Clouds and gases have emissivities which vary rapidly with wavelength. Certain bodies (e.g., the ocean) have emissivities near unity within certain spectral regions.

Emissivity is defined as the ratio of emitted radiation to that from an ideal blackbody (i.e., perfect emitter) at the same temperature. Therefore, if R is the emitted radiance and ε is the emissivity of the source, then $R = \varepsilon B$, where B is the Planck radiance.

Earth's radiance to space varies with wavelength in a non-uniform manner due to the existence of spectral absorption bands which cause abrupt variations in atmospheric transmission with wavelength. The various absorption bands are seen in fig. 1.2 which shows the transmittance of the entire atmosphere as a function of wavelength and the major constituents responsible for the various absorption bands. Thus, earth radiance to space varies with wavelength because (a) the Planck emission dependence on wavelength and (b) atmospheric transmission varies with wavelength. Moreover,

the dependence of radiance upon the temperature of the emitting source decreases with increasing wavelength (or increases with increasing wavenumber).

Before proceeding with a discussion of satellite remote sensing concepts it is important to define the reflectivity, transmissivity, and absorptivity of a radiating medium. Figure 1.3 presents a schematic of the processes involved. Here R_λ is the incident radiation, $r_\lambda R_\lambda$ is the reflected radiation, $a_\lambda r_\lambda$ is the absorbed radiation and $\tau_\lambda R_\lambda$ is the transmitted radiation. The emitted radiation is given by $\varepsilon B(T)$. Conservation of energy demands that the sum of the absorptivity (a), reflectivity (r), and transmissivity (τ) equal unity. For a blackbody medium, such as the earth's surface or a dense cloud, where $\tau=r=0$, the absorptivity is unity (the body is completely absorbing). Furthermore, for a body in local thermodynamic equilibrium ($\partial T/\partial t=0$), the thermal energy emitted must equal the energy absorbed ($\varepsilon_\lambda B_\lambda=a_\lambda R_\lambda$). If the source of radiation is in thermal equilibrium with the absorbing medium, then $R_\lambda=B_\lambda$ and $\varepsilon_\lambda=a_\lambda$. Thus results Kirchoff's Law, which states that "the sum of the emissivity, reflectivity, and transmissivity of a body in local thermodynamic equilibrium is unity ($\varepsilon+r+\tau=1$)." Kirchoff's Law is generally assumed to hold for the earth and its atmosphere. Furthermore, for the atmosphere the reflection of thermal radiation is negligible since the wavelength of radiation is large compared to the size of molecules. Therefore, for the atmosphere, the emissivity can be approximated by one minus the transmissivity ($\varepsilon=1-\tau$).

In review, the emissivity (ε) is defined as the ratio of the emitted radiant energy to that of an ideal blackbody at the same temperature; the absorptivity (a) is the ratio of absorbed radiant energy to the incident energy; the reflectivity (r) is the ratio of reflected radiant energy to the

incident energy; and the transmissivity (τ) is the ratio of transmitted radiant energy to the incident energy.

The transmittance of the atmosphere above any pressure level, p, is given by a probability function which represents the probability that a photon leaving that pressure level will reach space. Mathematically,

$$\tau(\nu,p) = \exp\left[-\frac{1}{g}\int_o^p k(\nu,p)q(p)dp\right] \tag{1.6}$$

where g is gravity, $k(\nu,p)$ is the absorption coefficient (a measure of absorption efficiency of the atmosphere at wavenumber ν), and $q(p)$ is the mixing ratio of the optically active gas(es) at wavenumber ν. In terms of optical depth $U(p)=1/g\int_o^p q(p)dp$,

$$\tau(\nu,p) = \exp\left[-k(\nu)U(p)\right] \tag{1.7}$$

where $K(\nu)$ is a mass weighted mean absorption coefficient $(K(\nu)=\int_o^p k(\nu,p)q(p)dp/\int_o^p q(p)dp)$.

1.8 Radiative Transfer Equation

The radiance leaving the earth-atmosphere system which can be sensed by a satellite borne radiometer is the sum of radiation emissions from the surface and from each atmospheric level that are transmitted to the top of the atmosphere. Considering the earth's surface to be a blackbody emitter (emissivity equal to unity) the upwelling radiance intensity, $I(\nu)$, for a cloudless atmosphere is given by the expression

$$I(\nu) = B(\nu,T_s)\tau(\nu,p_s) + \sum_p \varepsilon(\nu,p)B(\nu,p)\tau(\nu,p) \tag{1.8}$$

where the first term is the surface contribution and the second term is the atmospheric contribution to the radiance to space. Using Kirchoff's law, the emissivity of an infinitessimal layer of the atmosphere at pressure p is equal to the absorptivity (one minus the transmissivity) of the layer. Consequently,

$$\varepsilon(\nu,p)\tau(\nu,p) = [1-\tau(\nu,\delta p)]\tau(\nu,p) = \tau(\nu,p) - \tau(\nu,\delta p)\tau(\nu,p) \ . \qquad (1.9)$$

Since the transmittance is an exponential function of depth of the absorbing constituent

$$\tau(\nu,\delta p)\tau(\nu,p) = e^{-k\delta p}\, e^{-kp} = e^{-k(p+\delta p)} = -\tau(\nu,p+\delta p) \ . \qquad (1.10)$$

Thus

$$\varepsilon(\nu,p)\tau(\nu,p) = \tau(\nu,p) - \tau(\nu,p+\delta p) = -\Delta\tau(\nu,p) \qquad (1.11)$$

and

$$I(\nu) = B(\nu,T_s)\tau(\nu,p_s) - \sum_{p} B(\nu,p)\Delta\tau(\nu,p) \ . \qquad (1.12)$$

In integral form,

$$I(\nu) = B(\nu,T_s)\tau(\nu,p_s) - \int_{x(o)}^{x(p_s)} B(\nu,p)\, \frac{d\tau(\nu,p)}{dx(p)}\, dx(p) \qquad (1.13)$$

where $x(p)$ can be any function of pressure. For numerical quadrature reasons $x(p)$ is generally chosen as $\ln p$ or $p^{2/7}$. In (1.13): (1) $I(\nu)$ is the spectral radiance measured by the satellite at wavenumber ν, (2) the function $\tau(\nu,p)$ as given by (1.6) is the atmospheric fractional transmittance of the radiation from pressure level p to the top of the atmosphere; (3) the term

$B(\nu,T_s)\tau(\nu,p_s)$ is the spectral radiance emitted by the surface and attenuated by the atmosphere, often called the Boundary Term; (4) the integrated quantity is the spectral radiance emitted to space by the atmosphere.

1.9 Radiation flux (irradiance)

The radiance, $I(\nu)$, is the flux of radiant energy at a given wavenumber per unit time across unit area into a cone defined by the unit solid angle. Since the atmospheric radiation field is not usually homogeneous, it is necessary to define the radiance for increments of area and solid angle and to account for the angle θ between the direction of the radiance and the normal of the incremental area. Figure 1.4 illustrates the radiance geometry.

2.0 Surface Temperature

Until the launch of the TIROS-N operational satellite series, high spatial resolution radiometers operated in visible and infrared window regions primarily for the purpose of imaging the atmosphere's cloud cover. For example, the High Resolution Infrared Radiometer (HRIR) flown on the Nimbus I and II satellites in the early 1960's measured radiation from the earth with 4 mile resolution at 0.7 μm and 3.7 μm. The Scanning Radiometers (SR's) which flew on the operational NOAA satellites prior to the TIROS-N series, possessed 4 mile resolution in the 0.7 μm and 11 μm window regions. The AVHRR (Advanced Very High Resolution Radiometer) which flies on the TIROS-N series is the first high resolution instrument (1/2 mile) to possess both 3.7 μm and 11 μm window channels along with two visible channels. The five channel AVHRR on the NOAA satellites launched after 1981 carries a fifth channel at 12 μm, whose measured radiance is weakly absorbed by water vapor, to enable more precise corrections for atmospheric water vapor attenuation of the upwelling radiances observed by the window channels.

In the infrared, the emissivity of the earth's sea and land surface is near unity. As a result, in the absence of cloud or atmospheric attenuation, the brightness temperature observed with a space-borne window radiometer is equal to surface skin temperature. However, cloud and water vapor absorption usually prohibit direct interpretation of the window channel data so that algorithms need to be applied to the data to alleviate the influence of clouds and water vapor absorption. The algorithms and instrumental approach have evolved from the use of a single window channel on a polar orbiting satellite to the use of multi-spectral radiometer observations from both polar orbiting and geostationary satellites.

2.1 Selection of Cloudfree Observations

2.1.1 Single Channel Approaches

The first high resolution imaging devices possessed a single window channel. Statistical histogram techniques (Smith et al., 1970; and Brower et al., 1976) were used to separate cloud free observations from cloud contaminated observations for the purpose of obtaining sea surface temperature measurements.

The histogram technique is based upon the following assumptions:

1) Since sea surface temperature is slowly varying in space, cloud free IR window measurements over an area should be very repetitive. Thus, sea surface brightness temperature values will have a high frequency of occurrence.

2) Cloud contamination will produce lower than sea surface brightness temperature values and the cloud brightness temperatures will be highly variable over an area due to variations in cloud amount, opacity, and altitude.

The histograms of brightness temperature are formed from spatial samples of data containing about 1,000 measurements. This produces a single retrieval for a sample of data which covers a sea surface area having a linear dimension of about 250 km for the 8 km field of view of the scanning radiometer sensors. For the TIROS-N, 1.0 km resolution AVHRR, 1000 measurements are possible within areas having a linear dimension of only 30 km. In either case, there are enough samples to apply histogram techniques to the data in order to separate cloud-free observations from cloud contaminated observations.

The histogram situation is shown in fig. 2.1. Part (a) of fig. 2.1 shows the typical normal distribution obtained when all 1,000 measurements are cloud free, no SST gradient exists, and 1°C class intervals are used. Part (b), on the other hand, illustrates the situation when more than half of the 1,000 samples are cloud contaminated. Since the cloud-contaminated radiance temperatures are lower than the cloud free temperatures, they populate the left hand side of the histogram, but also distribute themselves normally. Only the warm side of the normal density curve formed by cloud free observations can be distinguished from the combined data in the histogram. Since the mean of the normal (Gaussian) density function (probability function) formed from clear observations is the most likely value of the SST, schemes were developed to infer the mean of a Gaussian probability function from knowledge of the standard deviation σ of the density function and knowledge of the geometry of one side of the distribution.

2.1.1.1 The Slope Method

Assume that the radiance (blackbody) temperature T over the cloud free portion of the sample of 1,000 observations has a normal density function of the form

$$f(T) = f_o \exp\left[-(T-T_o)^2/2\sigma^2\right] , \qquad (2.1)$$

where f is the frequency of occurrence, $f_o = f(T_o)$ is unknown, the standard deviation σ is assumed to be known from the characteristics of the measuring instrument, and the mean temperature T_o is the quantity to be determined. It is well known that the standard deviation of a normal probability density function occurs at the two inflection points on the curve, that is, where

$$\frac{df}{dT} = \max \quad \left(\text{hence, } \frac{d^2f}{dT^2} = 0\right). \tag{2.2}$$

Let T_m be the temperature at which (2.2) is satisfied. Then the desired SST is obtained from the relation

$$T_o = T_m - \sigma \, . \tag{2.3}$$

Now T_m is easily obtained by finding the point of maximum slope. The temperature at which this point occurs is then T_m, which when applied to (2.3) yields the sea surface temperature T_o. The σ in (2.3) has to be determined from the equation,

$$\sigma = (\sigma_N^2 + \sigma_E^2)^{1/2} \, , \tag{2.4}$$

where σ_N and σ_E are the standard deviations, respectively, of the instrument noise and the expected variance of the SST's.

2.1.1.2. The Three Point Method

As with the slope method, the three point method assumes the normal probability function of (2.1) and attempts to find T_o from the spatial sample of 1,000 measurements. However, in this method, no value for σ need be assumed; it is determined along with T_o. Begin with any three points (T_i, f_i),

(T_j,f_j), and (T_k,f_k) on the warm side of the histogram, which by (2.1) satisfy the three equations

$$f_i = f_o \exp\,[-(T_i-T_o)^2/2\sigma^2] \tag{2.5a}$$

$$f_j = f_o \exp\,[-(T_j-T_o)^2/2\sigma^2] \tag{2.5b}$$

$$f_k = f_o \exp\,[-(T_k-T_o)^2/2\sigma^2]. \tag{2.5c}$$

This simultaneous system of equations contains the three unknown quantities f_o, σ, and T_o and is solved by simple variable elimination. Thus eliminating f_o,

$$\ell n(f_i/f_j) = -[(T_i^2-T_j^2)-2T_o(T_i-T_j)]/2\sigma^2\ , \tag{2.6a}$$

$$\ell n(f_i/f_k) = -[(T_i^2-T_k^2)-2T_o(T_i-T_k)]/2\sigma^2\ , \tag{2.6b}$$

or, finally, after elimination of σ,

$$T_o = \frac{T_i^2\ \ell n(f_j/f_k) - T_j^2\ \ell n(f_i/f_k) + T_k^2\ \ell n(f_i/f_j)}{2[T_i\ \ell n(f_j/f_k) - T_j\ \ell n(f_i/f_k) + T_k\ \ell n(f_k/f_j)]}\ . \tag{2.7}$$

Since a single calculation of T_o from (2.7) can be influenced by noise and by the combination of the three points being slightly non-Gaussian, repeated calculations of T_o are made from all possible unique combinations of three points on the warm side of the histogram. Thus, if there are n useful points on the warm side, then the combinations: i=1,...,n-2; j=i+1,...,n-1; and k=j+1,...,n; are used to construct a second histogram, called the mean estimate histogram from which the most frequently occurring estimate is taken as the correct one.

Another procedure for selecting the SST is to construct a two dimensional histogram from the individual T_o and σ estimates. Then the T_o,σ combination having the greatest frequency of occurrence is adopted as being the most probable surface temperature and its standard deviation for the area of observation.

2.1.1.3 Least Squares Method

Another solution of the three point method is through a least squares fit of the normal distribution probability function to three or more points on the warm end of the observed frequency distribution. It follows from (2.1) that

$$\ell nf(T) = (\ell nf_o - \frac{T_o^2}{2\sigma^2}) + \frac{T_o}{\sigma^2}T - \frac{1}{2\sigma^2}T^2 , \qquad (2.8)$$

or

$$\ell nf(T) = A_o + A_1T + A_2T^2 , \qquad (2.9)$$

where

$$T_o = -A_1/2A_2 ,$$

and

$$\sigma = -1/2A_2 .$$

Thus, given three or more points (f_i,T_i) and the non-cloud contaminated portion of the histogram one can solve for T_o and σ using the least squares solution of (2.9).

2.1.2 Multi-spectral Cloud Filtering Methods

Shown in fig. 2.2 are histograms of IR brightness temperature measurements for two visible channel reflectance measurement categories; low reflectance (<15%) and high reflectance (>45%). Low reflectance measurements

will result from thin cirrus cloud or cloud free conditions, the two being easily separable in the infrared window measurements by the drastic difference in the emitting temperature of the high cold circus and the warm underlying surface. High reflectance measurements result from thick clouds at all levels. In this case the infrared brightness temperature provides a good indication of the cloud level. Intermediate reflectance data provide ambiguous target interpretations since they result from a mixture of cloud and surface contributions. In summary, for the purpose of estimating the surface temperature from infrared brightness temperature data, cloud contamination of the frequency distribution resulting from cloud free data can be minimized by eliminating all data for which the corresponding visible channel reflectances are greater than the expected cloud free reflectance values.

At night the difference between the brightness temperatures measured in the 3.7-4.0 μm and in the 10-11 μm window regions can be used to minimize the contamination of the clear mode of observations by partial cloud or thin cloud within the instrument's field-of-view. Small or negative differences are observed only for the case where an opaque scene (e.g., thick cloud or the surface) fills the field-of-view of the sensor. The negative difference at night results for the extended cloud condition due to the lower emissivity of cloud at 3.7 μm than at 11 μm. Moderate to large differences result if a non-uniform scene (e.g., broken cloud) is observed. The different spectral response to a scene of non-uniform temperature is a result of Planck's law; the brightness temperature dependence on the warmer portion of the scene increasing with decreasing wavelength.

With the advent of the multi-spectral window radiometer, cloud free fields of view could be selected on the basis of a number of "clear sky condition" measurement consistency tests. The brightness temperature data for

the clear fields of view over an area of interest are then checked for internal consistency, thereby eliminating erroneous estimates and averaging consistent estimates to obtain an area average SST. This approach was first tested with the 3.7 μm and 11 μm window channel data obtained from the Nimbus-5 ITPR (Smith et al., 1974) and was the basis for the multi-spectral window design of the TIROS-N series AVHRR which includes channels for measuring reflected sunlight in the visible (0.7 μm) and near infrared (0.9 μm) region of the spectrum as well as thermal infrared channels in atmospheric window spectral regions centered at 3.7 μm, 11 μm, and 12 μm.

The use of clear sky condition measurement consistency tests for the selection of cloud free fields of view for the processing of SST from TIROS-N/NOAA AVHRR data has been presented by McClain et al. (1982). The physical basis for the tests is summarized below.

2.1.3 Visible channel albedo tests

The albedo of the oceans and atmosphere is generally less than 10%, except in the direct glitter (specular reflection) regions, whereas the albedo of most clouds is greater than 50%. Thus, thresholds can be established that represent the expected bidirectional reflectance in the absence of clouds. The thresholds are not constant but varies with solar zenith angle, satellite zenith angle, and azimuth of the viewed spot. Bidirectional reflectance threshold tests are generally sensitive to even small amounts of cloudiness but are subject to error for at least two reasons: (1) the reflectance threshold tables may contain some residual cloud contamination; and (2) the true cloud free reflectance varies with atmospheric state (aerosols) and sea state (wave conditions).

Uniformity tests consist of comparing adjacent field of view (FOV) measurements in specific channels and requiring that they agree to within the

expected variation due to instrumental noise. Under partly cloudy conditions the variations are larger from differences in cloud amount, thickness, or height of the top surface than it is from noise in the data. The AVHRR instrument is well suited for performing uniformity tests because it is characterized by low noise and relatively high spatial resolution. Variations greater than 0.2°C within the three infrared channels are indicative of the presence of clouds, as are differences of more than 0.2 percent reflectance in the reflected sunlight channels. The uniformity tests can be applied to a small number of adjacent global area coverage (GAC) FOV's, e.g., a 2 x 2 array (about 8 kilometers on a side). Within such small arrays, variations of sea state (horizontal gradients of SST and glitter) and atmospheric state (horizontal gradients of water vapor and aerosols) are sufficiently small that uniformity tests are generally effective in the detection of clouds.

Uniformity cloud tests will fail at night in the presence of either a uniform cloud cover filling the FOV or a uniform distribution of clouds much smaller than the FOV. In these cases, a relationship between the three infrared window channels is needed that is nearly invariant with respect to the water vapor concentration, but which is strongly affected by the presence of clouds. As will be shown in section 2.2, a linear function of the temperature difference between any two window channels can be used to correct another window channel measurement for atmospheric attenuation. This result implies that with the multichannel AVHRR instrument one can obtain several invariant relationships for cloud free conditions, such as

$$a_1 + b_1 (T_{3.7} - T_{11}) + c_1 (T_{11} - T_{12}) = 0 , \qquad (2.10)$$

and

$$a_2 + b_2 (T_{3.7}) + c_2 (T_{11}) = 0 . \qquad (2.11)$$

In the presence of transmissive clouds or small sub-resolution cloud elements, the measured radiance is a combination of the Planck radiance of the cold cloud and the warm ocean surface. Because the Planck radiance is more sensitive to temperature in the 3.7 μm window than in the 11 μm or 12 μm windows, when inverting to brightness temperatures, the 3.7 μm will be highly elevated relative to the 11 μm or 12 μm temperatures. In the case of cirrus clouds, this elevation exceeds that associated with even the tropical cloud free condition and can easily exceed 20°C when the FOV is 80-90% filled with cloud.

In the case of thick non-transmissive clouds, the different sensitivity of the Planck radiances is insignificant. However, the optical properties of such clouds are significantly different at 3.7 μm than at 11 μm. Theoretical studies show that the reflectivity of thick water droplet clouds is greater at the 3.7 μm wavelength, the difference with respect to the 11 μm wavelength increases with decreasing water droplet size (Hunt, 1973). This lowers the 3.7 μm temperatures relative to the 11 μm temperatures much more than for cloud free conditions. Thus, the invariant relations (2.10 and 2.11) provide a means of cloud detection at night when the reflected sunlight channels cannot be used.

2.2 Water vapor correction

The surface temperature can be expressed in terms of the observed clear sky window channel brightness temperature, T_B, and a water vapor correction, ΔT:

$$T_S = T_B + \Delta T \qquad (2.12)$$

As a consequence of Planck's law, it can be shown that for the same degree of water vapor absorption, the water vapor correction is highly dependent upon wavelength. Considering Planck's law:

$$B_{\nu}(T) = \frac{c_1 \nu^3}{e^{c_2 \nu / T} - 1} \tag{2.13}$$

one finds that at 3.7 μm, the Planck radiance varies with temperature to approximately the thirteenth power whereas at 11 μm the Planck radiance varies with temperature to approximately the fourth power. Using a Planck radiance to temperature proportionally, $B(T) \sim T^n$, it can be shown that

$$T_B(\nu) \tilde{\sim} \{\tau_S(\nu) T_S^{\ n} + [(1 - \tau_S(\nu))] T_a^{\ n}\}^{1/n} \tag{2.14}$$

where τ_S, T_S, and T_a are the atmospheric transmittance, surface temperature, and effective atmospheric temperature, respectively. Assuming realistic values of 0.8, 300°K, and 270°K for τ_S, T_S, and T_a, respectively, one finds that at 3.7 μm where n=13, the brightness temperature observed is 296.5°K as opposed to a value of 294.5°K observed at 11 μm where n=4. Thus, for a non-isothermal condition and the same atmospheric transparency, the water vapor correction depends on wavelength.

2.2.1 Statistical Relations

There is a natural correlation of the difference between brightness temperature and ground temperature with the observed brightness temperature due to the fact that water vapor decreases with increasing cloud height and latitude (decreasing radiating surface temperature). This relation was utilized by Smith et al., (1970) to correct single channel water vapor window

brightness temperatures for water vapor attenuation. The correction took the form

$$\Delta T = a_o + a_1 T_B + a_2 T_B^2 \tag{2.15}$$

where the a_o, a_1, and a_2 coefficients were determined by regression analysis of a large sample of brightness temperatures synthesized from a climatological sample of atmospheric soundings.

Figure 2.3 illustrates the water vapor corrections derived for the Nimbus-2 satellite 3.7 μm channel and the 11 μm channel of the NOAA satellites. As can be seen, the correction for molecular absorption in the 11 μm region is about twice as large as that for the 3.7 μm region due to the Planck radiance dependence discussed above.

Unfortunately, the use of a single channel climatological correction proved to be inadequate for daily estimates of SST, especially in the tropics where the water vapor correction is large, highly variable in space and time, and not well correlated with the observed brightness temperature (Barnett et al., 1979).

2.2.2 Multi-window channel H_2O correction

Advanced instruments carry radiometers observing multiple window regions simultaneously. This enables an internal physically based correction for water vapor attenuation to be made. Consider the radiative transfer equation in the form:

$$I = B_S \tau(U_S) - \int_o^{U_S} B \frac{d\tau}{dU} dU \tag{2.16}$$

where I is the observed radiance, B is the Planck radiance, U is the precipitable water, and the S subscript denotes surface conditions. For window regions for which the absorption is weak,

$$\tau(U) \approx e^{-KU} \approx 1 - KU \tag{2.17}$$

where K, the absorption coefficient, is relatively small.

Thus,

$$I = B_S(1 - KU_S) + K\int_0^{U_S} B\,dU \tag{2.18}$$

Defining an atmospheric mean Planck radiance, $\tilde{B}$,

$$\tilde{B} = \int_0^{U_S} B\,du \Big/ \int_0^{U_S} dU = \frac{1}{U_S}\int_0^{U_S} B\,dU \ . \tag{2.19}$$

Then

$$I = B_S(1 - KU_S) + K\tilde{B}U_S \tag{2.20}$$

or

$$B_S - I = (B_S - \tilde{B})KU_S \ . \tag{2.21}$$

Since B_S is close to I and $\tilde{B}$ is close to B_S the following first order Taylor expansions can be used:

$$\begin{aligned} B_S - I &\approx \left(\frac{\partial B}{\partial T}\right)_S (T_S - T_B) \\ B_S - \tilde{B} &= \left(\frac{\partial B}{\partial T}\right)_S (T_S - \tilde{T}) \end{aligned} \tag{2.22}$$

where $\tilde{T}$ is the atmospheric mean temperature corresponding to $\tilde{B}$ as determined using the inverse of (1.3). Substituting (2.22) into (2.21) yields

$$T_S - T_B = (T_S - \tilde{T})KU_o \ . \tag{2.23}$$

Now consider two window wavelengths such that

$$\frac{T_S - T_B(W_1)}{T_S - T_B(W_2)} = \frac{K(W_1)}{K(W_2)} = \frac{K_1}{K_2} \ . \tag{2.24}$$

It then follows that

$$T_S = \frac{K_2}{K_2 - K_1} T_B(W_1) - \frac{K_1}{K_2 - K_1} T_B(W_2) \tag{2.25}$$

or

$$T_S = T_B(W_1) + \frac{K_1}{K_2 - K_1} [T_B(W_1) - T_B(W_2)] \ . \tag{2.26}$$

For three window channels (e.g., 4.0 μm, 11 μm, and 12 μm) it can be shown that

$$T_S = T(W_1) + \frac{K_1}{2(K_2 - K_1)} [T_B(W_1) - T_B(W_2)] + \frac{K_1}{2(K_3 - K_1)} [T_B(W_1) - T_B(W_3)] . \tag{2.27}$$

Figure 2.4 provides a graphical representation of the multispectral window channel water vapor correction algorithm. This linear extrapolation technique was first proposed by Anding and Kauth (1970) and initially tested by Prabhakara et al., (1974) using Nimbus satellite 11 μm and 13 μm window data. The application of the technique to TIROS-N/NOAA AVHRR data is

described by McClain et al., (1982). The technique is also being routinely applied to multi-spectral window radiometer data from the geostationary satellite VAS instrument (Bates, 1982).

2.2.3 Operational practice (1973-1983)

Daily routine processing of infrared data from NOAA's polar orbiting satellites for global sea surface temperatures began in December of 1972 (Brower et al., 1976). The Improved TIROS Operational Spacecraft (ITOS) of that period were equipped with a scanning radiometer that gathered visual (0.5-0.7 μm) data at 3.5 km resolution and thermal infrared (10.5-12.5 μm) data at 8 km resolution. For each 100 x 100 km array of scanspot temperatures judged to have a sufficient number of apparently cloud free scanspots to delineate a warm model the histogram technique (Smith et al., 1970) was used to determine the brightness temperature corresponding to this mode. Initially the brightness temperatures were corrected for atmospheric attenuation, using the statistical relationship to the observed brightness temperature and satellite viewing angle presented in fig. 2.3. After June of 1973 the brightness temperatures were corrected with coefficients derived from processing of coincident temperature and moisture profile soundings (500 km resolution) from the Vertical Temperature Profile Radiometer (VTPR) carried on the same spacecraft (McMillin, et al., 1973).

In 1976, a new statistical procedure was introduced that uses the full resolution (50 km) calibrated measurements from one or more channels of the VTPR (that were coincident with the SST determination from the NOAA satellite scanning radiometer) in a multiple regression equation for estimating atmospheric absorption effects (Walton et al., 1976). As part of this new processing method, it was also necessary to incorporate a parametric cloud detection procedure to isolate a set of clear SST determinations and associated VTPR measurements.

With the advent of the TIROS-N generation of NOAA operational satellites, in late 1978 SST processing was modified somewhat. The greatest initial changes stemmed from the 4 km resolution lower noise level radiometric data that were now available from the Advanced Very High Resolution Radiometer (AVHRR), and the use of the 25 km resolution HIRS (High Resolution Infrared Sounder) data for aid in cloud detection and for atmospheric corrections (Lauritson, et al., 1979). A statistical maximum likelihood technique (Crosby et al., 1978) was applied to 11 x 11 arrays of 11 μm data to provide the fundamental histogram-type cloud-free temperature estimates at a grid resolution of 50 km. A discriminant function type of cloud classifier was used to alleviate the influence of clouds on the SST estimates (Walton, 1980).

Beginning in 1981, the full multi-spectral capabilities of the AVHRR were utilized for SST determination (McClain et al., 1982). The selection of cloud free brightness temperature observations was based on the use of multi-channel radiance consistency tests as described in section 2.1.2. The water vapor correction is made using linear relations (eq. 2.27) between brightness temperature attenuation and the multi-spectral brightness temperature observations within the 3.7 μm, 11 μm, and 12 μm "windows" whose opacity increases with wavelength in this case.

Experimental SST products are available from the VISSR Atmospheric Sounder (VAS) on the GOES satellites (Smith, 1981 and Bates, 1982), and the Scanning Multi-channel Microwave Radiometer (SMMR) flown on Nimbus-7 (Wilheit and Chang, 1979). VAS SST estimates are obtained in the same manner as AVHRR estimates and are expected to be used operationally in the near future, especially in the tropics. The time continuity of observation and the small variation in viewing angle over a geographical region made possible by the geostationary orbit greatly assists the detection of the small but highly

significant thermal variations in tropical waters. Although the microwave measurement technique possesses the advantage of being able to sense through non-precipitating clouds, the required accuracy of 1°C for SST determinations has not yet been demonstrated. The operational SST specification technique will most likely evolve into an algorithm which combines the advantages of polar and geostationary satellite observations in both the infrared and microwave spectral regions.

3.0 Atmospheric soundings

3.1 Overview

The measurement of atmospheric profiles from satellite observations of thermal emission was proposed by King (1956), Kaplan (1959), and Wark (1961). The satellite vertical sounding program which followed was economically justified on the basis of its potential for improving numerical forecasts, large scale medium to long range (greater than 1 day), over continents as a result of improved observation over oceans. Forecast impact experiments conducted with global operational polar orbiting satellite sounding data sets during the First Global GARP Experiment (FGGE) demonstrate that this expectation has been realized (Bengtsson et al., 1982). More recently it has become apparent that satellite soundings can also play a key role in supplying the observations needed for small-scale intense weather prediction. This is a result of the high resolution (∿30 km) and the horizontal and temporal consistency of the data, the latter a result of the fact that the same instrument and processing scheme affect each measurement. Vertical soundings achieved from geostationary satellites are particularly useful for the local weather analysis/forecast operation since they provide the time continuity required for observing the rapid evolution of small scale weather disturbances. Because the demands for data accuracy and reliability become

increasingly critical as one attempts to decrease the scale of the observed and forecast phenomena and at the same time extend the range of prediction, sounding processing methods have evolved from purely objective methods into approaches which allow for direct interaction between the meteorologist and the data processing computer.

3.2 Basic considerations

3.2.1 Radiative transfer equation

The equation (1.13) governing the transfer of earth-atmosphere radiance to space was derived assuming that the surface of the earth was non-reflecting and opaque (i.e., $\varepsilon_\nu=1$). This assumption is generally valid for the infrared region of the spectrum but not for the microwave region of the spectrum, particularly over water where the surface reflectivity (and emissivity) is about 50%, depending upon sea state. The surface radiance to space in this case is

$$I_\nu(p_s) = \varepsilon_\nu B_\nu(T_S)\tau_\nu(0,p_s) + r_\nu\left[\int_{p_s}^{0} B_\nu[T(p)]\,\frac{\partial\tau_\nu(p_s,p)}{\partial p}\,dp\right]\tau_\nu(0,p_s) \qquad (3.1)$$

where the first term on the right-hand side denotes the surface emission transmitted to space and the second term represents the downward atmospheric emission which reflected by the earth's surface and transmitted to space. Substituting (3.1) into (1.13) for the surface contribution yields

$$I_\nu(\nu) = \varepsilon_\nu B_\nu(T_S)\tau_\nu(0,p_s) - \int_0^{p_s} B_\nu[T(p)]\left[(1-\varepsilon_\nu)\tau_\nu(0,p_s)\,\frac{\partial\tau_\nu(p_s,p)}{\partial p} + \frac{\partial\tau_\nu(0,p)}{\partial p}\right]dp \qquad (3.2)$$

where Kirchoff's law was employed to replace r_ν by $(1-\varepsilon_\nu)$. It can be shown that the transmittance for monochromatic radiation is an exponential function

of optical depth (1.6). Thus

$$\tau_\nu(p_s,p) = \exp\{-[\frac{1}{g}\int_{p_s}^{p} k_\nu(p)q(p)dp]\}$$

$$= \exp\{-[\frac{1}{g}\int_{p_s}^{0} k_\nu(p)q(p)dp - \frac{1}{g}\int_{p}^{0} k_\nu(p)q(p)dp]\}$$

$$\tau_\nu(p_s,p) = \tau_\nu(p_s,0)/\tau(p,0) = \tau_\nu(0,p_s)/\tau(0,p) \ .$$

Since $\tau_\nu(0,p_s)$ is independent of p,

$$\frac{\partial\tau_\nu(p_s,p)}{\partial p} = -\frac{\tau_\nu(0,p_s)}{\tau^2(0,p)}\frac{\partial\tau_\nu(0,p)}{\partial p} \ . \tag{3.3}$$

Substituting (3.3) into (3.2) yields

$$I_\nu(\nu) = \varepsilon_\nu B_\nu(T_S)\tau_\nu(0,p_s) + \int_0^{p_s} B_\nu(T)W_\nu(p)\frac{dp}{p} \tag{3.4}$$

where

$$W_\nu(p) = -\{1 - (1 - \varepsilon_\nu)[\frac{\tau_\nu(0,p_s)}{\tau_\nu(0,p)}]^2\}\frac{\partial\tau_\nu(0,p)}{\partial \ln p} \tag{3.5}$$

is the Planck radiance weighting function.

Thus, in the infrared region where $\varepsilon_\nu \tilde{\sim} 1$, the Planck radiance weighting function of the integral equation is simply given by the vertical derivative of the atmospheric transmittance function whereas in the microwave region where $\varepsilon_\nu \neq 1$, the weighting function is complicated by its dependence upon surface emissivity. For the sea surface, typical values of microwave surface emissivity range between 0.4 and 0.6, depending upon sea state. For land, typical values range between 0.8 and 1.0, depending upon soil moisture and vegetation cover.

Several spectral regions are considered to be useful for remote sounding from satellites as shown in fig. 3.1. There are windows, regions of minimal atmospheric absorption, near 4 μm, 10 μm, 0.3 cm and 1 cm wavelengths. These window regions are useful for sensing the temperature of the earth's surface and clouds, and in the case of the microwave window region, the surface emissivity and the liquid water content of the clouds. The CO_2 and O_2 absorption bands at 4.3 μm, 15 μm, 0.25 cm and 0.5 cm are useful for temperature profile sensing since the mixing ratios of these uniformly mixed gases are known. The water vapor absorption bands near 6.3 μm, beyond 18 μm, and near 0.2 cm and 1.3 cm are used for probing the atmosphere's water vapor concentration.

3.2.2 Physical basis

The outgoing radiation varies with wavenumber (wavelength) for two reasons: (a) the Planck function (blackbody radiance) dependence on wavelength and (b) the absorption by atmospheric gases whose spectral dependence is determined by the gas's molecular structure. The second reason (b) dominates the spectral variation of outgoing radiance over narrow spectral intervals. Radiation from the earth's surface and atmosphere is absorbed by various atmospheric gases in spectral bands, each absorption band consisting of numerous individual narrow absorption lines. At the band center where the lines are strongest, very little atmosphere is required for complete absorption. On the other hand, in the band wings where the lines are weak and the absorption is due mainly to the wings of stronger lines near the band center, a large path of atmosphere is required to absorb the incident radiation.

Thus, the concept of determining the vertical profile of an atmospheric parameter from spectral radiance measurements is based on the fact that

atmospheric absorption and transmittance is highly dependent upon the frequency of the radiation and the amount of the absorbing gas. At frequencies close to the centers of absorbing bands, a small amount of gas results in considerable attenuation in the transmission of radiation and therefore most of the outgoing radiation arises from the upper levels of the atmosphere. On the other hand, at frequencies which are far from the centers of the band a relatively large amount of absorbing gas is required to attenuate transmission; therefore, at these frequencies the outgoing radiation arises from the lower layers of the atmosphere.

For example, consider the Nimbus-4 IRIS spectrum (fig. 3.2) in the vicinity of the 15 μm CO_2 band. In the far wing ($\sim 800 cm^{-1}$) the upwelling radiance corresponds to a surface temperature of 320°K. Moving towards the center of the band, the radiation temperature decreases due to the decrease of temperature with altitude in the lower atmosphere. The minimum radiation temperature is around 210°K corresponding to emissions from the tropopause region and then the radiation temperature increases again to almost 240°K at the band center due to the fact that atmospheric temperature increases with altitude in the stratosphere.

Figure 3.2 makes the problem of obtaining temperature profiles of the atmosphere appear deceivingly simple. Unfortunately, upwelling radiance sensed at each of the particular frequencies arises from a large vertical depth of the atmosphere. The radiative transfer equation (3.4) shows that the radiance observed from the atmosphere is a mean "blackbody radiance" weighted by the function $w_\nu(p)$.

Figure 3.3 shows the Planck radiance weighting functions for seven channels of a sounding spectrometer flown on an experimental satellite in 1969. As may be seen, the radiance arises from deep (~10 km thick) and

overlapping layers. Because of the large depth contributing to the outgoing radiance measurements, there is no unique relation between the spectrum of outgoing radiance and the details of the vertical temperature profile. Also, because of the large degree of overlap of the weighting functions of neighboring spectral intervals, the radiance observations are not independent of each other. Both the non-uniqueness and lack of independence of the spectral radiance observations with respect to the vertical temperature profile cause serious difficulties in the inverse solution of the radiative transfer equation for the temperature (or absorbing gas) profile.

3.3 Analytical Methods of Retrieval

There is no unique solution for the detailed vertical profile of temperature or an absorbing constituent because; (1) the contribution to the earth-atmosphere outgoing radiances arise from relatively deep layers of the atmosphere, (2) the contribution to the radiances observed within various spectral channels overlap considerably such that the observations contained in a set of spectral radiances are not vertically independent of each other, and (3) measurements of outgoing radiance possess errors. As a consequence, there are a large number of analytical approaches to the profile retrieval problem. The approaches differ both in the numerical procedure for solving the set of spectrally independent radiative transfer equations (e.g., matrix inversion versus iteration) and in the type of ancillary data used to constrain the solution to insure that a meteorologically meaningful result is achieved (e.g., the use of atmospheric covariance statistics as opposed to the use of an apriori estimate of the profile structure). There are some excellent papers in the literature which review the retrieval theory which has been developed over the past few decades (e.g., Fleming and Smith, 1971; Fritz et al., 1972; Rodgers, 1976; and Twomey, 1977). The intent of this section is to

present the mathematical basis for procedures which have been utilized in the operational retrieval of atmospheric profiles from satellite measurements without discussing the details of their use for any particular satellite instrument configuration.

3.3.1 General Considerations

Accurate retrieval of atmospheric temperature and moisture profiles ultimately depends upon the ability to describe the measurements by the radiative transfer equation, (3.4). For a practical instrument whose spectral channels have a finite spectral bandwidth, all quantities given in (3.4) are integrated over wavenumber being weighted by the spectral response of the instrument. However, since B varies slowly with ν while τ varies rapidly and without correlation to B within the narrow spectral channels of the sounding spectrometer, it is sufficient to perform the spectral integrations of B and τ independently and treat the results as if they are monochromatic values for the effective wavenumber, ν_j. Analytically

$$B(\nu_j,T) = \frac{\int_0^\infty B(\nu,T)\phi_j(\nu)d\nu}{\int_0^\infty \phi_j(\nu)d\nu} \text{ and } \tau(\nu_j,p,\theta) = \frac{\int_0^\infty \tau(\nu,p,\theta)\phi_j(\nu)d\nu}{\int_0^\infty \phi_j(\nu)d\nu} \qquad (3.6)$$

where $\phi_j(\nu)$ is the spectral response of the j^{th} spectral channel. In practice, $B(\nu_j,T)$ and $\tau(\nu_j,p,\theta)$ are empirically modeled as functions of T and p on the basis of exact calculations for a variety of atmospheric conditions. This facilitates rapid calculation of atmospheric radiances during the profile retrieval process. (See Smith et al., 1974; McMillin and Fleming, 1976; and Fleming and McMillin, 1977 for a description of the Planck radiance and atmospheric transmittance function modeling techniques).

3.3.2 Temperature Profile Retrievals

3.3.2.1 Linearization

For temperature profile retrievals the boundary term of the radiative transfer equation is usually handled separately. For example, in the case of the infrared ($\varepsilon_s \tilde{\nu} 1$), the surface skin temperature is defined from multispectral window radiometer measurements as described in section 2.0. In the case of microwave sounding channels, the surface emissivity is specified using brightness temperature measurements in window channels (e.g., 30 GHz) and relationships for the spectral variation of emissivity for land or sea surface conditions. In any event, subtracting the known boundary contribution from the observed radiance measurement yields

$$I'(\nu) = \int_0^{p_s} B_\nu(T) W_\nu(p) \frac{dp}{p} . \tag{3.7}$$

In treating infrared measurements it is necessary to linearize the dependence of Planck radiance on temperature. This is generally done by using a first order Taylor expansion about a mean condition. Defining the mean temperature profile condition as $\overline{T}(p)$, we have

$$B_\nu(T) = B_\nu(\overline{T}) + \frac{\partial B_\nu(T)}{\partial T} (T - \overline{T})$$

and (3.8)

$$I(\nu) = \overline{I}(\nu) + \frac{\partial B_\nu[T_B(\nu)]}{\partial T_B(\nu)} [T_B(\nu) - \overline{T}_B(\nu)] .$$

Substituting (3.8) into (3.7) yields

$$T_B'(\nu) = \int_0^{p_s} T'(p) W_\nu^*(p) \frac{dp}{p} \tag{3.9}$$

where $T_B'(\nu)=T_B(\nu)-\overline{T}_B(\nu)$, $T'(p)=T(p)-\overline{T}(p)$, and

$W_\nu^*(p)=W_\nu(p)[\partial B_\nu(T)/\partial T]/[\partial B_\nu(T_B)/\partial T_B]$. Dropping the superscript notation and considering the observational error, $\varepsilon(\nu)$, the radiative transfer equation to be solved is

$$T_B(\nu) = \int_0^{p_s} T(p) W_\nu(p) \frac{dp}{p} + \varepsilon(\nu) \tag{3.10}$$

Written in numerical quadrature form, we have

$$T_i^B = \sum_{j=1}^{N} W_{ij} T_j + \varepsilon_i \qquad i=1,2,\ldots,M \tag{3.11}$$

where M is the number of spectral channels and N the number of level temperatures.

3.3.2.2 Direct Inverse Solution

Equation (3.11) written in matrix notation is

$$t_b = Wt + \varepsilon \tag{3.12}$$

where capital letters denote matrices and lower case letters denote vectors. One can solve for the temperature profile, t, by multiplying (3.12) by W^{-1},

$$t = W^{-1}t_b + W^{-1}\varepsilon \tag{3.13}$$

Equation (3.13) represents the solution of M equations for M unknown T_j values. Unfortunately, this direct solution is unstable with respect to the influence of the unknown observation error because W is nearly singular due to strong overlapping of the weighting functions. Since W is ill-conditioned with respect to matrix inversion, the elements of the inverse matrix are

greatly inflated, which in turn greatly amplifies the experimental error of the observations. This renders the solution useless. In other words, the ill-conditioned solution results from the fact that one does not have N independent pieces of information about T from M radiation observations. The solution is further complicated because M is usually much smaller than the number of temperature points, N, needed to represent the temperature profile.

3.3.3 The Use of Basis Functions

Let

$$T(p_j) = \sum_{k=1}^{L} a_k f_k(p_j) \tag{3.14}$$

where $L \leq M$ and $f_k(p_j)$ are some type of basis function (e.g., polynomials, the weighting functions $W_\nu(p)$, or empirical orthogonal functions).

An empirically optimal approximation is achieved by defining $f_k(p_j)$ as empirical orthogonal functions (EOF) which are the eigenvectors of a statistical covariance matrix $T^T T$. That is, the eigenvector and associated eigenvalues of $(T^T T)$ are determined and the N eigenvalues are ordered from largest to smallest, the associated eigenvectors will be ordered according to the amount of variance they explain in the empirical sample of soundings used to determine $T^T T$. The "EOF's" are optimal basis functions in the sense that the first EOF=$f_1(p_j)$ is the best single predictor of T(p) that can be found in a mean squared error sense to describe the values used to form $T^T T$. The second EOF is the best prediction of the variance unexplained by $f_1(p_j)$, and so on. Wark and Fleming (1966), first used the EOF approximation in the RTE (3.11) to obtain

$$T_i^B = \sum_{k=1}^{L} a_k \left[\sum_{j=1}^{N} W_{ij} f_{kj} \right] + \varepsilon_i$$

$$T_i^B = \sum_{k=1}^{L} a_k H_{ik} + \varepsilon_i \ , \tag{3.15}$$

or in matrix notation

$$T_b = Ha + \varepsilon \ .$$

If L<M, say L=M/2 then ε can usually be ignored and one can use the least squares solution for a,

$$a = (H^T H)^{-1} H^T t_b \ . \tag{3.16}$$

(In practice the empirical function series is truncated either on the basis of the smallness of the eigenvalues (i.e., explained variances) of higher order eigenvectors or on the basis of numerical instabilities which result when L approaches M.)

If L≤M and L is small (e.g., ≤5), a stable solution can usually be obtained by the direct inverse

$$a = H^{-1} t_b . \tag{3.17}$$

The matrix H in this case is much less singular (better conditioned with respect to matrix inversion) than is W. This is because the basis vector f_k is smooth and acts as a constraint on the solution thereby stabilizing it. However, in practice, best results are obtained by choosing an optimum L<M or by conditioning the H matrix prior to its inversion (Wark and Fleming, 1966).

3.3.4 Least Squares Regression

The least squares regression solution was used for the operational production of soundings from the very first sounding spectrometer data (Smith et al., 1970). Consider the form of the direct inverse solution (3.13) where t_b are observations which include the measurement error (i.e., $t_b = t_b + \varepsilon$), then

$$t = w^{-1} t_b \text{ or } t = t_b A \tag{3.18}$$

where A is a matrix of solution coefficients. One can define A as that matrix which gives the best least squares solution for t in a statistical ensemble of simultaneously observed radiances and temperature profiles. Extending (3.18) to an entire sample of K soundings, where K>>M and N,

$$T = T_b A \ , \tag{3.19}$$

where the matrices T and T_b have dimensions of K x N and K x M, respectively. It follows that

$$T_b^T T = T_b^T T_b A$$

and

$$A = (T_b^T T_b)^{-1} T_b^T T \tag{3.20}$$

where the superscript T indicates matrix transposition.

The advantages of the regression method over other methods are: (1) if one uses real radiance and radiosonde data matchups to form the statistical sample, one does not require knowledge of the weighting functions or the observation errors, (2) the instrument need not be calibrated in an absolute sense, and (3) the regression is numerically stable.

Some shortcomings of the regression method are: (1) it disregards the physical properties of the RTE in that the solution is linear whereas in fact the exact solution is non-linear because the weighting function W and consequently the solution coefficients A are functions of temperature, (2) the solution uses the same operator matrix for a range of radiances depending upon how the sample is stratified, and thus the solution coefficients are not situation dependent, and (3) radiosonde data is required, so that a radiosonde

network must be maintained. An eigenvector regression method (Smith and Woolf, 1976) is used in the processing of operational TIROS-N series satellite sounding data. The method combines the advantages of regression and empirical orthogonal function expansions.

3.3.5 Statistical Regularization

To make explicit use of the physics of the RTE in the statistical method, one can express the brightness temperatures (3.12) for the statistical ensemble of profiles as

$$T_b = TW + E \ , \tag{3.21}$$

where E is a matrix of the unknown observational errors. Substituting (3.21) into (3.20) yields

$$A = (S^T T^T TW + E^T E)^{-1} W^T T^T T \ . \tag{3.22}$$

In deriving (3.22), covariances between observation error and temperature ($E^T T$) are assumed to be zero since they are uncorrelated. Defining the covariance matrices

$$S_t \equiv \frac{1}{K - 1} (T^T T) \text{ and } S_e \equiv \frac{1}{K - 1} (E^T E) \tag{3.23}$$

then

$$A = (W^T S_t W + S_e)^{-1} W^T S_t \tag{3.24}$$

The solution for the temperature profile is available from (3.18)

$$t = t_b (W^T S_t W + S_e)^{-1} W^T S_t \text{ or } T_j = \sum_{i=1}^{M} T_i B_{c_{ij}} \tag{3.25}$$

This solution was developed independently by Strand and Westwater (1968), Rodgers (1968), and Turchin and Nozik (1969).

The objections raised about the regression method do not apply to this statistical regularization solution; namely, (1) W is included and its temperature dependence can be taken into account through iteration, (2) the solution coefficients are reestablished for each new temperature profile retrieval, and (3) there is no need for coincident radiosonde and satellite observations so that one can use a historical sample to define S_t. The advantages of the regression method are, however, the disadvantages of the statistical regularization method; namely, (1) the weighting functions must be known with high precision, and (2) the instrument must be calibrated accurately in an absolute sense. As with regression, the statistical regularization solution is stable because S_t and S_e are strongly diagonal matrices which makes the matrix $(S^T S_t W+S_e)$ well conditioned for inversion.

3.3.6 Minimum Information Solution

Twomey (1963, 1965) using the minimum information case of Foster (1961) developed a temperature profile solution to the radiances which represents a minimal perturbation of a guess condition, for example, a forecast profile. In this case t represents deviations of the actual profile from the guess and t_b represents the deviation of the observed brightness temperatures from those which would have arisen from the guess profile condition. S_t is then a covariance matrix of the errors in the guess profile, which is unknown. Assume that the errors in the guess are uncorrelated from level to level such that

$$S_t = \sigma_t^2 I \tag{3.26}$$

where I is the identity matrix and σ_t^2 is the expected variance of the errors in the guess. If one also assumes that the measurement errors are random,

then

$$S_\varepsilon = \sigma_\varepsilon^2 I \tag{3.27}$$

Substituting (3.26) and (3.27) into (3.25) yields

$$t = t_b (W^T W + \gamma I)^{-1} W^T \tag{3.28}$$

where $\gamma = \sigma_\varepsilon^2 / \sigma_t^2$ ($\tilde{\gamma} 10^{-3}$). The solution given by (3.28) is the Tikhonov (1963) method of regularization.

The solution (3.28) is generally called the Minimum Information Solution since it requires only an estimate of the expected error of the guess profile. One complication of this solution is that γ is unknown. However, one can guess at γ (e.g., 10^{-3}) and iterate it until the solution converges,

$$\frac{1}{M} \sum_{i=1}^{M} (T_i^b - \hat{T}_i^b)^2 \leq \sigma_\varepsilon^2 \ . \tag{3.29}$$

The minimum information solution was used for processing sounding data by the SIRS-B and VTPR instruments aboard the Nimbus-4 and ITOS-D series of satellites, respectively (Smith, Woolf and Fleming, 1972).

3.3.7 Non-linear Iterative Solutions

Consider the RTE in the form of (3.7)

$$r(\nu) = I'(\nu) = I(\nu) - B_\nu(T_s)\tau_\nu(p_s) = \int_0^{p_s} B_\nu[Tp] W_\nu(p) \frac{dp}{p} \tag{3.30}$$

3.3.7.1 Chahine Method

Using the mean value theorem

$$r(\nu) = B_\nu[\tilde{T}(p)] \int_0^{p_s} W(\nu,p)\,dp \tag{3.31}$$

where $\tilde{p}$ corresponds to the pressure of some level within the area encompassed by the weighting function for which the temperature satisfies the mean value approximation.

Then

$$\frac{r(\nu)}{\hat{r}(\nu)} = \frac{B[\nu,T(\tilde{p})]}{B[\nu,\hat{T}(\tilde{p})]} \tag{3.32}$$

where $\hat{T}(p)$ represents a "guess" profile condition. This leads to the successive approximation formula

$$B(T_i^n) = B(T_i^{n-1}) \frac{r_i}{r_i^{n-1}} \tag{3.33}$$

where

$$B(T_i^n) = B[\nu_i, T^n(\tilde{p}_i)]$$

$$r_i = r(\nu_i)$$

$$r_i^{n-1} = \int_0^{P_s} B[\nu_i, T^{(n-1)}(p)] W_\nu(p) \frac{dp}{p}$$

Chahine's original scheme (Chahine, 1968) was to assume that $\tilde{p}_i$ was that pressure at the peak of the weighting function. Thus one solved for the same number of temperatures as the number of radiance observations.

The numerical process of Chahine's retrieval scheme can be summarized as follows:

1) Pick a $T^{(o)}(p)$ and compute r_i^o for i=1,2,...,M
2) Compute $B(T_i^o)$ for i=1,2,...,M
3) Use measurements r_i with r_i^o and $B(T_i^o)$ to get $B(T_i^1)$
4) Invert the Planck function to get M values of T_i^1
5) Interpolate M values of T_i^1 to get a continuous profile
6) Repeat steps 2-5 until convergence, $(1/M) \Sigma (r_i - r_i^n)^2 \leq \sigma_\varepsilon^2$.

The major problems with the Chahine method are: (a) the profile is not usually well represented by a series of line segments between pressure levels where the weighting functions peak, particularly for a small number of channels (levels), and (b) if the iteration is not stopped at the point where the convergence criterion is satisfied, the solution will become unstable since one is attempting to extract M distinct pieces of information from M non-independent observations; that is, the solution will suffer the same disaster as the direct matrix inversion solution (3.13).

3.3.7.2 Generalized Iterative Method

A generalization of the Chahine scheme was developed by Smith (1970) to avoid specifying solution points and to insure numerical stability while achieving the solution. Instead of using the approximation (3.32), one uses

$$B(T_{ij}^{\,n}) = [B(T_{ij}^{\,n-1}) + (r_i - r_i^{\,n-1})] \tag{3.34}$$

where

$$B(T_{ij}^{\,n}) = B[\nu_i T^{(n)}(p_j)] \ , \ i=1,2,\ldots,M; \ j=1,2,\ldots,N$$

Therefore, at each step one can solve for a corrected temperature for all levels from the radiance residual in each channel. The best estimate of the temperature at each iterative step is then given by a weighted average of the results achieved for each channel, where the weight is chosen to be the temperature profile weighting function of the RTE. That is,

$$T^{(n)}(p_j) = \sum_{i=1}^{M} T_{ij}^{\,(n)} W_{ij} \Big/ \sum_{i=1}^{M} W_{ij} \ . \tag{3.35}$$

The weight W_{ij} can be further modified by its division by the expected observational error to provide a closer fit of the solution to the more accurate radiance observations. The convergence criteria utilized is

$$\frac{1}{M} \Sigma \, (r_i^{\,n} - r_i^{\,n-1})^2 < \frac{\sigma_\varepsilon^{\,2}}{10} \, . \tag{3.36}$$

The advantages of the generalized iterative method are; (a) no interpolation required, (b) the solution is stable in the averaging scheme (3.35), because the random error propagating from r into T is suppressed to the average value of the errors amongst all channels which will tend to be near zero, and (c) one doesn't have to know the measurement noise at all.

The main disadvantage is that the averaging process occasionally prevents obtaining a solution that satisfies the observations to within their measurement error levels. One method of overcoming the smoothing characteristic of the iterative solution is to couple this solution with a direct matrix inverse method (e.g., minimum information) whereby the iterative solution provides the first guess profile. The coupled iterative-direct matrix inversion method is used for the routine processing of geostationary satellite sounding observations (Smith, 1983).

3.3.8 Water Vapor Profile Retrievals

Water vapor profiles can be derived from radiance observations using methods similar to those used for the temperature profile determination. In the case of the infrared, multi-spectral observations in the 6.3 μm H_2O absorption band and in the 18-50 μm region of the rotational H_2O absorption band are used for profile determinations. In the microwave spectrum, measurements along the wing of a very strong absorption line at 183 GHz can be used for water vapor profiling. Total precipitable water vapor concentration

can be determined from split window channels in the infrared and microwave regions of the spectrum. The term split window is used to denote two neighboring channels in a relatively transparent (i.e., window) region of the spectrum; one channel for which the atmosphere is relatively transparent and the other for which atmospheric water vapor is less transparent to the surface radiance to space. In the infrared, 11 μm and 12 μm satisfy the split window requirements, whereas in the microwave, 30 GHz and 20 GHz are used.

3.3.8.1 Total Water Vapor Estimation

The use of microwave split window brightness temperature measurements over oceans provides a relatively accurate measure of the total water vapor concentration (Staelin et al., 1976, and Grody, 1976). In this case, two microwave spectral channels possessing different opacities to water vapor are used to separate the contributions to the measured brightness temperatures by water vapor and by liquid water. The solutions for the total water vapor concentration (U) and total liquid water concentration (Q) has been shown by Staelin et al. (1976) to be of the form

$$U = u_0 + u_1 T_B(\nu_1) + u_2 T_B(\nu_2)$$

and (3.37)

$$Q = q_0 + q_1 T_B(\nu_1) + q_2 T_B(\nu_2)$$

where the u and q coefficients are dependent upon the frequencies utilized and to a lesser degree on surface temperature and emissivity which are relatively constant for the sea. Standard practice is to obtain the coefficients of (3.37) by regression analysis of brightness temperatures computed from prescribed temperature profile, water vapor profile, surface temperature, surface emissivity, cloud, and precipitation conditions. Results of this

approach achieved with Nimbus-5 and Nimbus-6 22 GHz and 31 GHz brightness temperature data over oceans exhibit an accuracy of about 10% (Staelin et al., 1976; and Grody et al., 1980).

The microwave split window technique does not work well over land because the brightness temperature measurements are overly sensitive to the surface emission rather than atmospheric water substance emission, resulting from the high (but variable) surface emissivity.

The split window method can be used to specify total water vapor concentration from clear sky 11 μm and 12 μm brightness temperature measurements. The solution results from (2.23),

$$U = \frac{T_S - T_B(\nu)}{k(\nu)[T_S - \tilde{T}(\nu)]} . \tag{3.38}$$

It is evident from (3.38) that the accuracy in the determination of the total water vapor concentration depends upon the contrast between the surface temperature, T_S, and the effective temperature of the atmospheric emission, $\tilde{T}(\nu)$. In an isothermal situation, the total precipitable water vapor concentration is indeterminate.

The solution to (3.38) is achieved using the split window approximation for surface temperature (2.25),

$$T_S = \frac{k(\nu_2)T_B(\nu_1)}{k(\nu_2) - k(\nu_1)} - \frac{k(\nu_1)T_B(\nu_2)}{k(\nu_2) - k(\nu_1)}$$

and by expressing $\tilde{T}(\nu)$ as proportional to T_S,

$$\tilde{T}(\nu) = \alpha(\nu)T_S . \tag{3.39}$$

Then evaluating (3.38) for $\nu=\nu_1$ yields

$$U = \frac{T_B(\nu_1) - T_B(\nu_2)}{[1 - \alpha(\nu_1)][k(\nu_2)T_B(\nu_1) - k(\nu_1)T_B(\nu_2)]} \tag{3.40}$$

or

$$U = \frac{T_B(\nu_1) - T_B(\nu_2)}{u_1 T_B(\nu_1) - u_2 T_B(\nu_2)} . \tag{3.41}$$

As in the case with microwave observations, the coefficients u_1 and u_2 can be solved by linear regression analysis of (3.41) in the form

$$T_B(\nu_1) - T_B(\nu_2) = u_1 T_B(\nu_1) U - u_2 T_B(\nu_2) U \tag{3.42}$$

where the brightness temperatures are computed from prescribed temperature and water vapor profile conditions or are observations coincident with in-situ (e.g., radiosonde) observations of U. The weakness of the method is due to the time and spatial variability of $\alpha(\nu)$ and the insensitivity of a stable lower atmospheric state when $T_B(\nu_1) \tilde{\nu} T_B(\nu_2)$, there is little sensitivity to the total precipitable water vapor concentration. The influence of variations in the surface skin to air temperature ratio can be minimized by using localized statistics or by solving (3.42) for u_1 and u_2 from brightness temperatures computed from a prescribed surface temperature and temperature profile condition for two extreme water vapor concentration profiles. To facilitate the latter approach, the water vapor mixing ratio profile is prescribed by the power law model

$$w(p) = W(p_o) \left(\frac{p}{p_o}\right)^{\lambda} \tag{3.43}$$

for which the total precipitable water is

$$U = \frac{1}{g} \int_0^{p_o} w(p)\, dp = \frac{w(p_o) P_o}{q(\lambda+1)} . \tag{3.44}$$

One has the choice of varying $w(p_o)$, λ, or both. For example, if the surface mixing ratio is known, then two extreme values of λ (e.g., λ=1, and λ=5) can

be used to create two sets of brightness temperatures and total water vapor concentration values from which the coefficients u_1 and u_2 can be determined by direct solution of (3.42). These coefficients can then be used in (3.41) with the brightness temperature observations to solve for the actual total moisture concentration.

The sensitivity of the split window observations to water vapor concentration improves during the daylight hours as the surface and boundary layer temperatures increase with solar heating. The split window method has proved to be valuable in creating high spatial resolution images of the water vapor concentration from the geostationary satellite VAS observations. These images can be used to monitor the time evolution of the mesoscale water vapor features associated with the development of afternoon and evening convective storms (Chesters et al., 1982).

3.3.8.2 Profile Solution

The radiative transfer equation (3.9) can be written in terms of the precipitable water vapor profile as

$$T_B'(\nu) = \int_0^U T'(u) W_\nu^*(u)\,du \qquad (3.45)$$

where the prime denotes a departure from a mean or initial profile condition and

$$W_\nu^*(u) = \left(\frac{\partial B_\nu(T)/\partial T}{\partial B_\nu(T_B)/\partial T_B}\right) \frac{\partial \tau(u)}{\partial u}$$

for an opaque surface. For microwave channels seeing the surface $W_\nu^*(u)=W_\nu(p)/[\partial u/\partial \ln p]$ where $W_\nu(p)$ is given in (3.6).

3.3.8.2.1 Linear Direct Method

One manner of solving (3.45) for the water vapor profile from a set of spectrally independent water vapor radiance observations is to employ one of

the linear direct temperature profile solutions discussed in section 3.3.2. In this case, however, one solves for the function T(u) rather than T(p). Given T(p) from a prior solution of carbon dioxide and/or oxygen channel radiance observations, u(p) can be found by relating T(p) to T(u). The mixing ratio profile, w(p), can then be obtained by taking the vertical derivative of u(p) (i.e., $w(p)=g\partial u/\partial p$).

Rosenkranz et al. (1982) have applied this technique to microwave measurements of water vapor emission. They used the regression solution for both the temperature versus pressure and temperature versus water vapor concentration profiles. The regression solutions have the form

$$T(p_j) = t_o(p_j) + \sum_{i=1}^{N} t_i(p_j) T_B(\nu_i) \tag{3.46}$$

and

$$T(u_k) = t_o(u_k) + \sum_{\ell=1}^{M} t_{\ell(uk)} T_B(\nu_\ell) \tag{3.47}$$

where $T_B(\nu_i)$ are brightness temperature observations of oxygen emission and $T_B(\nu_\ell)$ are brightness temperature observations of water vapor emission and $t_i(p_j)$ and $t_\ell(u_k)$ are the regression coefficients corresponding to each pressure and water vapor concentration level. U(p) is found from the intersections of the T(p) and T(u) profiles obtained by interpolation of the discrete values given by (3.46) and (3.47). An advantage of the linear regression retrievals is that they minimize the computer requirements for real-time data processing since the regression coefficient matrices are predetermined. For this reason an eigenvector regression method is currently used for global processing of TIROS-N water vapor radiance data (Smith and Woolf, 1976).

3.3.8.2.2 Non-linear Iterative Method

Various non-linear iterative retrieval methods for inferring water vapor profiles have been developed and applied to satellite water vapor spectral radiance observations; for example, Conrath (1969), Smith and Howell (1971), and Hayden et al. (1981). The formulation of the approach given below follows that given by Smith (1970).

Integrating (3.9) by parts enables one to write

$$T_B(\nu) - T_B^n(\nu) = \int_0^{p_s} [\tau(\nu,p) - \tau^n(\nu,p)] Q^n(\nu,p) \frac{dp}{p} \tag{3.48}$$

where

$$Q^n(\nu,p) = \left[\frac{\partial B_\nu(T)/\partial T}{\partial B_\nu(T_B)/\partial T}\right] \frac{\partial T}{\partial \ln p}$$

and the n superscript denotes the n^{th} estimate of the profile condition. Expanding $\tau(\nu,P)$ as a logarithmic function of the precipitable water vapor concentration, U(p) yields

$$\tau(\nu,p) - \tau^n(\nu,p) = \frac{\partial \tau(\nu,p)}{\partial \ln U^n(p)} \ln \frac{U(p)}{U^n(p)} .$$

Using the approximation

$$\frac{\partial \tau(\nu,p)}{\partial \ln U^n(p)} = \tau^n(\nu,p) \ln \tau^n(\nu,p)$$

which is valid for an exponential transmission function (1.6), then

$$T_B(\nu) - T_B^n(\nu) = \int_0^{p_s} \ln \frac{U(p)}{U^n(p)} W_w^n(\nu,p) \frac{dp}{p} \tag{3.49}$$

where

$$W_w^n(\nu,p) = \tau^n(\nu,p)\ \ln \tau^n(\nu,p)\left[\frac{\partial B_\nu(T)/\partial T}{\partial B_\nu(T_B)/\partial T}\right]\left(\frac{\partial T}{\partial \ln p}\right) .$$

Following the same strategy employed in generalized iterative temperature profile solution (3.35), it follows from (3.49) that from each water vapor channel brightness temperature an estimate of the ratio of the true precipitable water vapor profile with respect to the n^{th} estimate can be calculated using

$$r^n(\nu_i) = \frac{U(p)}{U^n(p)} = \exp \frac{T_B(\nu_i) - T_B^n(\nu_i)}{\int_0^{p_s} W_w^n(\nu_i,p)\ \frac{dp}{p}}$$

An average estimate of the precipitable water vapor profile based upon all water vapor channel estimates is then

$$U^{n+1}(p_j) = U^n(p_j)\left\{\frac{\sum_{i=1}^{I} W_w^*(\nu_i,p_j) r^n(\nu_i)}{\sum_{i=1}^{I} W_w^*(\nu_i,p_j)}\right\} . \qquad (3.50)$$

As in the temperature profile solution

$$W_w^*(\nu_i,p_j) = W_w^n(\nu_i,p_j)/\varepsilon(\nu_i) .$$

Now the mixing ratio profile, q(p), is related to the precipitable water according to the relation $q(p)=g\partial u(p)/\partial p$ where g is gravity. It follows that $q^{n+1}(p)$ can be estimated from $U^{n+1}(p_j)/U^n(p_j)$ as determined from (3.50) and

from $q^n(p_j)$ using

$$q^{n+1}(p) = q^n(p)\left[\frac{U^{n+1}(p)}{U^n(p)}\right] + gU^n(p)\frac{\partial}{\partial p}\left[\frac{U^{n+1}(p)}{U^n(p)}\right] \qquad (3.51)$$

The advantage of using (3.51) to compute q(p) is that the second term on the right hand side of (3.51) is small compared to the first term so that numerical errors produced by the vertical differentiation are small.

3.3.9 Cloud Limitations

Clouds are generally opaque to infrared radiation and transparent to microwave radiation. Because of available technology, infrared sounders were developed prior to the microwave sounding system. However, because of the cloud imposed limitations of infrared soundings, the evolution of the operational satellite has been towards an all-microwave sounding capability. For example, on the TIROS-N series the basic sounding unit is a 20 spectral channel High-resolution Infra-Red Sounder (HIRS) assisted by a four spectral channel Microwave Sounding Unit (MSU). By the year 1990, the polar orbiting operational satellites (the Advanced TIROS-N) will carry a 20 spectral channel Advanced Microwave Sounding Unit (AMSU) capable of improved temperature and water vapor soundings under all cloud conditions, thereby rendering the infrared HIRS obsolete. The replacement of the operational geostationary satellite infrared sounder (VAS) with an all-microwave sounder will be much slower because of the technical difficulty of achieving high spatial resolution from geostationary altitude using a microwave receiver of a practical size.

Techniques for dealing with clouds in the infrared have been developed and discussed in the literature (Smith, 1968; Smith et al., 1970; Chahine, 1974; Smith and Woolf, 1976; McMillin and Dean, 1982). The techniques generally employ three different approaches:

1) Searching for cloudless fields-of-view,

2) Specifying cloud top pressure and sounding down to cloud level as in the cloudless case, and

3) Employing adjacent fields-of-view to determine the clear sky signal from partly cloudy observations.

3.3.9.1 Clear Search

Methods of screening cloud-free fields-of-view of an infrared sounder for the profile retrieval process generally make use of: (a) visible channel reflectance data, (b) surface temperature analyses, (c) ancillary microwave sounding radiance observations, and (d) consistency between the 4.0 μm and 11 μm window brightness temperatures. Some typical tests used to judge an infrared sounder's field-of-view to be free of cloud contamination are:

(a) $r \leq a_s + 2\varepsilon_a$, where r is a visible channel reflectance observed by the sounding spectrometer, a_s is the expected surface albedo, and ε_a is the expected uncertainty of the surface albedo estimate.

(b) $\hat{T}_s \leq T_s + 2\varepsilon_T$, where $\hat{T}_s$ is the surface temperature predicted from the split-window observations of the sounder (see section 1.2), T_s is an estimate of the surface temperature usually obtained from analysis of prior satellite, buoy, and ship observations, and ε_T is the expected error of the estimated temperature value.

(c) $\hat{T}_B(MW) \leq T_B(MW) + 2\varepsilon_{MW}$, where $\hat{T}_B(MW)$ is the brightness temperature of a lower tropospheric sounding microwave channel predicted from the infrared brightness temperature observations using a regression relationship valid for clear sky conditions, $T_B(MW)$ is the observed microwave brightness temperature, and ε_{MW} is the expected error of the regression estimate for clear sky conditions.

(d) $|T_B(4\mu m) - T_B(11\ \mu m)| \leq 2\varepsilon_{\Delta T}$, where $T_B(4\ \mu m)$ is the brightness temperature observed in a 4 μm window channel, $T_B(11\ \mu m)$ is the brightness

temperature observed in an 11 μm window channel, and $\varepsilon_{\Delta T}$ is the expected difference between the two window channels for cloudless sky conditions.

The usual procedure is to subject the data to as many of the above tests as possible and then to simply average the clear field-of-view radiances within the area for which a sounding is desired. If no "clear field-of-views" are found then an approach which deals with cloud contaminated radiances must be taken.

3.3.9.2 Partial Cloud Solution

Techniques of exploiting the spatial fluctuations of radiances observed over a broken cloud condition to define the clear air radiance to space have been described by Smith (1968, 1974, and 1976), Chahine (1974), and McMillin and Dean (1982). The main principle is that broken clouds produce greater spatial variation of the radiance to space than do other atmospheric properties, especially over small horizontal distances. Thus, for a radiometer of sufficiently high spatial resolution, it can be shown (Smith, 1968) that the clear air radiance arising from an area possessing broken clouds at a uniform altitude is

$$I_c(\nu) = \frac{I_1(\nu) - n^* I_2(\nu)}{1-n^*} \tag{3.52}$$

where $I_1(\nu)$ and $I_2(\nu)$ are two spatially independent but geographically close observations of the radiance to space from the area of interest, and n* is the ratio of cloud amounts (n_1/n_2) for the two geographically independent fields of view of the sounding radiometer. Given an independent measurement of the surface temperature and measurements I_1 and I_2 in a spectral window, then n* can be determined and used to solve for I_c in different spectral channels. Another approach to determining n* is to use simultaneous microwave

observations (Smith and Woolf, 1976) and regression relations between a lower tropospheric microwave sounding brightness temperature and the associated infrared brightness temperatures observed for cloud free conditions.

The partly cloud n* solution has been the basis of the design of all operational infrared sounders (e.g., VTPR, ITPR, HIRS, and VAS). It is primarily for this reason that these operational infrared sounding instruments have been designed to scan the earth contiguously and with relatively high spatial resolution.

3.3.9.3 Overcast Cloud Condition

In overcast cloud conditions, sounding radiance information is limited to the atmosphere above the cloud. There are various techniques for using such observations to determine atmospheric profiles down to cloud level or to amalgamate these observations with simultaneous microwave sounding radiances in order to specify profiles down to the surface. The most common technique is to use a microwave or other ancillary temperature profile estimate to specify cloud corrections to the observed infrared radiance observations (Smith et al., 1970, 1976). In this case, two of the most transparent spectral channel infrared observations must be used to specify the height and amount of the cloud.

The clear air radiance, $I_c(\nu)$, can be shown to be (Fritz et al., 1972),

$$I_c(\nu) = I(\nu) + \alpha Q(\nu, p_c) \tag{3.53}$$

where α is effective cloud amount (product of cloud emissivity and fractional coverage) within the instrument's field-of-view, and

$$Q(\nu, p_c) = \int_{p_c}^{p_s} \tau(\nu, p) \frac{\partial B_\nu(p)}{\partial p} dp \ . \tag{3.54}$$

Using two relatively transparent and therefore cloud sensitive carbon-dioxide channel radiance observations (or alternatively a window and a carbon-dioxide channel observation), p_c and α can be determined from the equalities

$$\frac{Q(\nu_1,p_c)}{Q(\nu_2,p_c)} = \frac{I_c(\nu_1) - I(\nu_1)}{I_c(\nu_2) - I(\nu_2)} \text{ and } \alpha = \frac{I_c(\nu) - I(\nu)}{Q(\nu,p_c)} \tag{3.55}$$

by using the initial temperature profile to calculate $I_c(\nu)$ and $Q(\nu,p_c)$. Once p_c is known, then $Q(\nu,p_c)$ can be calculated for all the spectral radiance observations and used with α in (3.53) to correct all the sounding radiance observations for cloud attenuation.

The accuracy of the method is dependent upon the accuracy of the initial profile below the cloud. Thus, the method works well for low level cloud situations and deteriorates with increasing cloud height. Nevertheless, the method was used extensively for the operational processing of low spatial resolution SIRS infrared data (Smith et al., 1970, 1972) and is currently in use for the processing of geostationary satellite VAS infrared sounding radiance observations over extensive low level overcast clouds (Smith, 1983).

3.4 Operational Practice (1969-1983)

Beginning just one month after the launch of Nimbus-3 (April 1969), the very first satellite sounding spectrometer observations (SIRS-A) were processed operationally using the regression method (Smith, Woolf, and Jacob, 1970). The regression coefficients were calculated from samples of upwelling radiance observations and coincident conventional soundings. Corrections for clouds, high terrain, and hot terrain were calculated and applied to the observed radiances. The regression coefficients were based on a two week sample of data which was dynamically updated every day. The method had the

advantage that the results were dependent only upon the stability of the calibration, rather than its absolute accuracy, and no explicit information about the atmospheric transmittances was required, except for correcting the radiances for cloud and terrain influences.

For the SIRS-B on Nimbus-4, the "minimum information" retrieval method was employed operationally beginning in June, 1970 (Smith, Woolf, and Fleming, 1972). A 12-hour forecast produced routinely by the National Meteorological Center (NMC) was used as the first guess. Corrections for cloud and terrain influences were also made to the SIRS-B data. Although the SIRS-B data processing was conceptually simpler than for the SIRS-A, since no regression analysis was required, considerable effort was necessary to empirically tune the atmospheric transmittance functions used in the profile retrieval process.

Beginning in October, 1972, operational soundings were achieved from the VTPR flown on the ITOS-D series of NOAA satellites. The VTPR achieved a contiguous earth coverage of measurements with sufficiently high spatial resolution that clear air soundings could be defined under partly cloudy sky conditions. Unfortunately the absolute calibration accuracy of the measurements was not sufficient to use the minimum information physical retrieval method in the operational processing of the data. Instead, the regression method was employed (McMillin et al., 1973). Even though the VTPR possessed much higher spatial resolution than its SIRS predecessor, the radiometric precision was inferior and as a net result no significant improvement in sounding accuracy was realized.

The TIROS-N Operational Vertical Sounding (TOVS) system (Smith et al., 1979) with its high precision High-resolution Infra-Red Sounder (HIRS), the first operational Microwave Sounding Unit (MSU), and a Stratospheric Sounding Unit (SSU), provided a great improvement in satellite sounding accuracy. The

method of retrieval used for the operational processing of the data was that of eigenvector regression (Smith and Woolf, 1976). Refinements of the methods used for treating clouds were implemented by McMillin and Dean (1982).

An experimental processing system utilizing manual interaction in the TIROS-N sounding retrieval process was developed in order to provide high quality soundings at mesoscale spatial resolution (Smith et al., 1978, and Greaves et al., 1979). The approach utilizes the McIDAS interactive processor and video display system developed by the Space Science and Engineering Center at the University of Wisconsin (Suomi et al., 1982). The interactive processing system differs from the operational system in that an operator, by inspecting a video image of cloud cover and thermal radiance patterns constructed from the HIRS and MSU data, selects those individual fields-of-view of the TOVS best suited for sounding retrieval. The operator can ensure that adequate coverage of sounding data is achieved in the critical regions of the disturbed atmosphere. As is done objectively in the operational system, one of three types of retrievals (clear, partly cloudy or overcast) can be selected by the operator, depending upon cloud condition. Numerous display programs have been developed to enable the operator to recognize and delete erroneous TOVS soundings on the basis of meteorological inconsistencies. The erroneous data are recognized from either internal horizontal inconsistencies or inconsistencies with other meteorological data (e.g., rawinsonde) that are displayed with the TOVS soundings on a television monitor at the McIDAS operator's terminal. The end result is a dense network of meteorologically consistent TOVS soundings.

The interactive processing system was developed by a joint group of National Environmental Satellite Service (Development Laboratory) and University of Wisconsin (Space Science and Engineering Center) scientists to

process direct readout TOVS data over North America as part of a research program for improving the detection of the antecedent conditions of localized severe weather. In this application, hourly surface data are used to enhance the TOVS product. The processing system also served as a prototype of the system developed for processing high spatial and temporal resolution sounding data achieved from geostationary VAS satellites.

The first of a series of infrared sounding instruments (VAS) on operational geostationary satellites was orbited in September, 1980. The data have been processed routinely at the University of Wisconsin using a purely physical (as opposed to empirical regression) retrieval method which is a hybrid of the generalized iterative method (3.3.7.2) and direct matrix inversion (Smith, 1983). The results are obtained on McIDAS and made available to several operational centers (i.e., the National Meteorological Center, the National Severe Storms Forecast Center, and the National Hurricane Center) as part of a NOAA Operational VAS Assessment (NOVA) program (Schmidt et al., 1982). Some of the current capabilities of the VAS are: (1) high spatial resolution (15-75 km) vertical soundings of temperature and moisture with high temporal frequency (1-3 hours), (2) high accuracy (better than 1°K) surface skin temperature fields (Bates, 1982), and (3) greatly improved wind field determinations (Menzel, Smith, and Stewart, 1982). The VAS data processing and product dissemination system is planned to be fully operational by 1986.

3.5 Examples of Satellite Sounding Capabilities

3.5.1 Polar Orbiting Satellites

Polar orbiting satellite sounding data is primarily used as input to the global numerical weather analysis/prediction operation. For this purpose, satellite sounding observations are essential for the production of effective

forecasts in the Southern Hemisphere and contribute to an extension (by up to a day) of useful skills in numerical forecasts for the Northern Hemisphere. Most important, it appears that as a result of satellite soundings there is no longer a need for radiosonde stations at remote locations which are very expensive to maintain.

An example demonstration of the fidelity of the operational satellite global sounding capabilities is provided in fig. 3.4. Shown is a comparison of two completely independent analyses of the 1000-500 mb thickness valid at nearly the same time; one is an analysis of only satellite soundings achieved by a time assimilation of the asynoptic data (Smith et al., 1981), and the other is the analysis produced operationally by the NMC using all data available over the sea within ±3 hours of synoptic time, but excluding satellite soundings over land areas. As can be seen, the overall agreement of the two independent analyses is surprisingly good, especially over land areas where the data utilized in each analysis are entirely different (satellite as opposed to radiosonde). The example comparison serves to demonstrate the capability of the polar orbiting satellite sounding system to observe the synoptic scale details of the global mass distribution as needed to initialize extended range numerical prediction models.

3.5.2 Geostationary Satellites

The geostationary satellite VAS sounding capability is leading to significant improvements in short term local forecasting, especially the forecasting of severe convective storms. This is the result of the ability of the VAS system to sound the atmosphere with both high spatial and high temporal resolution.

Figure 3.5a shows a full disc image of cloudiness observed with the visible and infrared window spectral channels of the VAS. Such images have

been achieved by all geostationary meteorological satellites prior to the VAS. The VAS enables imagery of atmospheric carbon dioxide and water vapor emissions as well as clouds and these multi-spectral images are useful for delineating the thermal, moisture, and motion structure of the atmosphere. An example image of water vapor emission is shown in fig. 3.5b which was observed at exactly the same time as the cloud image of fig. 3.5a. In fig. 3.5b, the light areas correspond to regions of high upper tropospheric relative humidity whereas the dark areas correspond to regions of low upper tropospheric relative humidity (Smith and Zhou, 1982). Sharp boundaries of moisture are associated with baroclinic zones, such as upper tropospheric jet streams and storm boundaries. For example, the narrow moist band stretching across North America from the Great Lakes into Southern California is associated with a subtropical jet stream which is invisible in the cloud image shown in fig. 3.5a. Also, note that the circulation features of storms (e.g., the storm over the North Atlantic) are much better delineated in the water vapor imagery than in the cloud imagery.

The ability of the VAS to fill in important spatial gaps in the conventional network of balloonsonde water vapor observations is shown in fig. 3.5c. Shown is an analysis of 300 dewpoint values achieved from a high density of VAS soundings over Missouri and its bordering states. (The spacing of the VAS soundings is about 50 km.) The analysis is superimposed over the image of upper tropospheric water vapor emission observed with a resolution of 15 km. Also shown are balloon observations at the same time as the satellite observations. As can be seen, important spatial details of the water vapor distribution which cannot be resolved by the coarse network of balloon observations can be derived from the satellite measurements; for example, the moist band along the Illinois-Iowa border.

For forecasting severe convective weather, the temporal as well as spatial resolution of the data is of key importance. An example of the application of VAS soundings to the forecasting of severe convective storms is shown in fig. 3.6. Portrayed are analyses of various parameters derived from VAS soundings produced in real-time on April 26, 1982. Figure 3.6a illustrates mid-morning (10:00 a.m. LST) analyses of total precipitable water vapor (solid contours) and 300 mb gradient wind isotachs (dashed contours) over an image of upper tropospheric water vapor. Several meteorological features important for the development of convective weather can be seen in this illustration. In the first place there is an axis of high lower tropospheric water vapor (i.e., total precipitable water) extending from the Gulf of Mexico northward across Georgia. As can be seen from the water vapor image, this axis intersects a narrow zone of dry upper tropospheric air stretching across central Alabama indicating that the atmosphere over central Alabama is convectively unstable. Furthermore, isotachs of 300 mb gradient wind indicate that the core of the upper level jet is positioned over Louisiana and Mississippi with the exit region being over Alabama. The indirect circulation within the exit region of the upper level jet stream supports the continued destabilization of the atmosphere by the differential advections of warm moist Gulf air under cooler and drier upper tropospheric air (Uccellini and Johnson, 1979).

The stability of the atmosphere is portrayed in fig. 3.6 by analyses of the Total-totals Index (defined by the difference between the sums of the 850 mb temperature and dewpoint and twice the 500 mb temperature). As may be seen, Georgia is free of convective clouds at 1555 GMT but is overlaid by very convectively unstable air. For forecasting convective storms, the probability of thunderstorms increases as the Total-totals value exceed 50°C, with the

likelihood of severe thunderstorms and tornadoes increasing when the values exceed 60°C. As can be seen from fig. 3.6b, VAS soundings early in the day indicate the likelihood of severe thunderstorms over mid to southeastern Alabama. As shown in fig. 3.6c and 3.6d, the VAS soundings portrayed further destabilization of the atmosphere over Georgia. By 2000 GMT (fig. 3.6d) the Total-totals over southeastern Alabama approached 70°C indicating a very high probability of extensive severe weather in this area. As can be seen from the imagery, lines of convective storms had already developed over Georgia. During the six hour period subsequent to the 2000 GMT VAS observations, extensive severe weather occurred over Alabama and western Georgia, including thirteen tornadoes. Ground based reports indicated that 80% of the severe weather was within a triangle formed by Montgomery, Alabama, Birmingham, Alabama, and Columbus, Georgia, which is nearly coincidental with the 69 Total-totals contour shown in fig. 3.6d.

3.6 Other Sounding Systems and Future Prospects

There have been several limb-scanning radiometers and pressure modulated gas-cell radiometers flown on the Nimbus series of satellites for monitoring the temperature and gas composition of the stratosphere (Houghton, 1978 and Gille, 1979). One great advantage of the limb scanning radiometers is that they achieve much higher vertical resolution than a downward viewing device because of the much more rapid increase in optical depth with pressure and the symmetry of the geometrical path about the tangent point (fig. 3.7). The disadvantage of the limb-scanning approach is that the contribution to the observed radiance arises from a relatively large horizontal slice of the atmosphere ($\sim$500 km) and that the probability of receiving unwanted contributions from clouds is extremely high if the tangent point of the observed ray path is below the tropopause. For this reason, the technique has

been restricted to the observation of the upper atmosphere which is free of clouds and where the horizontal variability of temperature is rather small compared to the troposphere.

The future holds promise for significant improvements in sounding performance from satellites. During the late 1980's an Advanced Microwave Sounding Unit (AMSU) may replace the MSU on the TIROS-N series of polar orbiting satellites. The AMSU consists of fifteen spectral channels for measuring the temperature profile of the troposphere and stratosphere with a horizontal resolution of 50 km and five spectral channels for measuring the waver vapor profile with a horizontal resolution of 15 km. Theoretical studies indicate that the sounding performance of the AMSU will exceed that of the TOVS under all weather conditions, and especially in the presence of total cloud cover. Also the AMSU will be the first operational radiometer capable of sounding the water vapor profile through clouds.

Beyond the AMSU there exist other possibilities for improving the performance of sounding systems through instrumentation using both advanced passive and active techniques. Existing candidates in the category of advanced passive techniques are the Advanced Meteorological Temperature Sounder (AMTS) proposed by the NASA Jet Propulsion Laboratory (Kaplan et al., 1977, and Chahine, 1979) for future polar orbiting satellites and the High-resolution Interferometer Sounder (HIS) proposed by NOAA/NESDIS and the University of Wisconsin (Smith et al., 1979, and Smith, 1981) for future geostationary satellite applications. Both instruments operate in the infrared with extremely high spectral resolution ($\Delta\nu=0.0005\nu$) in order to achieve improved vertical resolution. In addition, the HIS provides a very sensitive measurement of the fine scale spectral structures of the emission to space resulting from fine scale vertical atmospheric structure. This is

possible through the use of optimal scanning of interferogram resonances produced by the regular spacing of the rotational fine structure lines of the CO_2 absorption bands. Temperature and moisture profile accuracies exceeding 1°C and 10%, respectively, appear possible with these advanced passive sounding radiometers.

Although no specific system proposal has been funded at the time of this writing, it now appears technically feasible to place a high spatial resolution millimeter wavelength microwave radiometer in geosynchronous orbit. A three meter diameter antenna would yield spatial resolutions of about 60 km, 30 km, and 20 km for the temperature profile measurements at 60 GHz and 120 GHz, and water vapor profile measurements at 180 GHz, respectively. Although the microwave sounder would not achieve the vertical and horizontal resolutions of the HIS, its cloud penetration capability would optimize the geostationary satellite sounding input to mesoscale numerical weather prediction models as well as enhance the shorter subjective/statistical predictions (nowcasting) of local weather.

Active techniques using laser, microwave, and radar transmitters are, in theory, the most effective means of remotely sounding the atmosphere with very high vertical and horizontal resolutions. Systems have been proposed using laser stimulation of Raman backscatter and multi-frequency Differential Absorption Laser (DIAL) methods of profiling temperature (Mason, 1975; Gill et al., 1979; Smith and Platt, 1977; and Korb and Wang, 1982) and water vapor (Browell et al., 1981; Browell, 1982; and Browell et al., 1983) but the technology and experimental demonstration of concepts are in an early stage of development. Moreover the active methods require power levels not contemplated for operational satellites in the near future.

4.0 Cloud Motion Winds

(Frederick R. Mosher, Space Science and Engineering Center, University of Wisconsin, 1225 West Dayton Street, Madison, Wisconsin, 53706)

Although tracking clouds in satellite pictures is one of the newest ways to measure wind, from another point of view it is also one of the oldest methods. C. F. Marvin in 1896 stated, "Observations and studies of clouds, their forms, heights, velocities, and direction of motion, constitute at present perhaps the most important source of information as to what is going on in the upper atmosphere." Winds determined from observations of cloud drift found uses in a number of studies. The International Cloud Year of 1896-97 was devoted to synoptic observations of cloud drift from which monthly mean averages were computed (Biglow, 1904). Information derived from cloud winds had strong impact on studies of the structure of cyclones. For example, Douglas (1922) used cloud winds to determine the upper air structure associated with the Norwegian cyclone model of Bjerknes. He showed the existence of troughs with cyclones and divergence aloft above the cyclonic centers. However, lack of knowledge of the mechanisms of upper air dynamics limited the use of cloud drift winds for forecasting purposes. Pick and Bowering (1929) concluded that cirrus direction may be only a fair indicator of the direction of depressions and that the cirrus velocity has little relationship to the depression velocity.

Radiosondes supplanted cloud drift observations for measuring wind, so by the 1950's very few cloud drift measurements were made. Still, the three-quarters of the globe covered by ocean remained essentially devoid of upper air measurements in spite of weather ships and transoceanic aircraft. The development of the geostationary meteorological satellite in the late 1960's revived the concept of using clouds as tracers of air motions. In a

sequence of images from a geostationary satellite, the clouds move. This motion is due to the wind at the level of the clouds. By tracking those clouds which move with the wind, it is possible to describe the motions of the atmosphere over oceans and other data-sparse regions.

The technology for obtaining cloud-tracked winds from geostationary images has progressed rapidly since 1966, when the first geostationary meteorological satellite, the Applications Technology Satellite (ATS-1), was launched. Cloud-tracked winds presently form a part of the Atlantic and eastern Pacific operational data base used by the National Meteorological Center for daily forecasts. The cloud-tracked winds played a major role in the Global Atmospheric Research Program (GARP) Global Weather Experiment. Measurements around the globe were provided by geostationary satellites operated by the United States, Japan, and the European Space Agency.

4.0.1 Cloud Tracking from Satellites

To obtain winds from cloud drift observations, one needs the following:

- A series of satellite images with good geometric fidelity
- A system to receive and store the satellite data
- Information on the earth location of the data being processed
- A system to process the satellite data
- A method of identifying a tracer cloud
- A method for determining the cloud height
- Techniques for quality control.

4.1 Geostationary Satellites

A satellite in geostationary orbit stays in the plane of the equator and completes one orbit per day in the same direction as the rotation of the earth. The effect of this orbit is to fix the satellite over the same location so that a series of images of the earth can be obtained.

Cloud tracking requires greater geometric image fidelity than can be obtained from a television camera, so all meteorological geostationary satellites use what is known as a spin-scan camera. As the satellite spins at a rate of about 100 rotations per second, a small telescope attached to a photomultiplier tube sweeps across the earth. One line of an image is made for each rotation of the satellite. The telescope "steps" down a line after each sweep. Line by line, the whole earth is scanned. It takes about 20 minutes to scan the entire earth, after which the telescope goes back up to the top and starts all over again.

4.1.1 Image Motions

The advantage of the geostationary image data is that one can follow the meteorological data over time. The sequence of images can be made into a movie loop which produces a sensation of image motion. If the images are aligned, the motions of the clouds are quite apparent. If the satellite were in a perfect geostationary orbit, all the images would naturally be aligned. However, the meteorological geostationary satellites are not in perfect orbits, so the images taken by the satellites have a tendency to move. The inclination of the orbit relative to the equator, the inclination of the spin axis of the satellite relative to the spin axis of the earth, and the eccentricity of the orbit all cause apparent motions in the satellite image sequences. The spin axis of the satellite is fixed in space, and the image plane is perpendicular to this spin axis. If the orbit is slightly inclined relative to the equator, the center of the image moves north and south during the day, as is shown by fig. 4.1. And if the spin axis of the satellite is inclined relative to the spin axis of the earth, the images again appear to move up and down and back and forth during the day (fig. 4.2).

Another apparent motion of the image is caused by the elliptical shape of the orbit. If the orbit were perfectly circular, the speed of the satellite would be constant. However, with an elliptical orbit the satellite moves faster when it is closer to the earth than when it is further away from the earth. That is, when the satellite is at the perigee (the orbit point closest to the earth), it is moving faster and gets ahead of earth's rotation. But when the satellite is at the apogee (the point of the orbit farthest away from the earth) it is moving more slowly and the earth's rotation gets ahead of the satellite. Hence the effect of the elliptical shape of the orbit is to cause an apparent east-west motion of the center of the image with a 24 hour period. The net effect of the motions due to elliptical orbits, orbit inclination and spin axis attitude is that the satellite images make a figure-eight pattern.

A further complication of the apparent motions is that the satellite's orbit and spin axis attitude are slowly changing, owing to the gravitational pull of the moon, sun, and larger planets; the force of the solar wind on the satellite; and other minor causes of orbital perturbations. The orbit changes slowly over a matter of weeks to months, but the net effect is that daily operations require updated information on where the satellite is looking, for purposes of image alignment and image gridding.

4.2 Image Navigation

To use a satellite image, one needs to know the earth location of the feature of interest. Since the earth moves around within the image plane of the satellite because of orbit effects, one needs to know where the satellite is at any time and how it is oriented in space. The process of determining where the satellite is and using this information to make a mathematical transformation from the satellite image coordinate system to an earth coordinate system is known as "navigation."

Groups at NASA, NOAA, and the University of Wisconsin have developed techniques to determine the orbit and attitude of the geostationary satellite for use in navigation processes. While the technique developed by Wisconsin (Hambrick and Phillips, 1980) is one of the simpler approaches, it has been the most successful. NASA is using it for geostationary data processing and NOAA will use it to produce image grids and aligned sequences used operationally by the NOAA National Environmental Satellite Service (NESS).

The Wisconsin system assumes that the satellite's orbit is known, that the satellite's attitude (the satellite's orientation in space) is slowly changing with time, and that the satellite is very seldom disturbed with repositioning maneuvers. The system uses an initial orbit measured by NASA tracking, refines the orbit to the accuracy required for image processing, and then propagates the orbit in time with a simple elliptical orbit model. The attitude is determined by measuring a single landmark (a geographic feature on the earth) over a series of five to seven images. With a known orbit and attitude it is possible to compute the nominal location of any point in an image. Since the orbit and attitude vary slowly with time, a simple plot of the history of the orbit and attitude parameters measured each day over a few weeks can be used to extrapolate these parameters forward in time with the use of simple curve-fitting techniques (Young, 1976). These orbit and attitude parameters can then be used predictively to grid the images and to align images or preselected sectors of images as they are received.

The absolute accuracy of the 24 hour parameters predicted by the Wisconsin technique is within approximately two full-resolution picture elements (2 km at the point below the satellite) of true earth location. The relative alignment error between successive images is much less than a full-resolution visible picture element. Thus full-resolution visible images can be ingested and aligned in real time for cloud-tracking purposes, with negligible error resulting from misalignment.

4.3 Storing and Processing the Satellite Data

The volume of data produced by geostationary satellites is much greater than that produced by most other types of meteorological sensors. All the surface and upper air measurements from conventional sources for the entire globe constitute about 10^7 bits of information each day. The ATS-type geostationary satellite (which operated from 1966 to 1974) generated about 6×10^9 bits of data each day. The current GOES (SMS) series of satellites generates more than 8×10^{10} bits per day for each satellite. That is the equivalent of 385 computer tapes per day. Storage of this much information is a problem, but access to the data is an even bigger problem. A cloud which could serve as a tracer is only a very small percentage of the total data volume (0.0004% of an image), so a lot of data need to be ignored in order to extract the information required to track a cloud.

The original approach to tackling the data volume and access problems was to use photographic images. The large volume of data could easily be stored, and all one needed to do to access the information was to look at it. Figure 4.3 shows an ATS-3 photograph image from 18 April 1972. Putting several images together in a movie loop produced the sensation of motion which could be followed by the eye. Movie loops of satellite images are frequently shown to the public on television weather shows. Projecting the images on a digitizing table makes it possible to measure the displacements of the clouds between images. This technique of manually measuring cloud motions by using movie loops is currently being used by NESS to measure cloud drift to obtain upper level winds operationally (Young, 1975).

While photographic images have advantages in that they are cheap and easily used with minimal equipment, they have many disadvantages. The camera lens produces some geometric distortions, the original brightness resolution

of the images depends on the strength of the developing solution, the manual alignment of the photographic images is difficult if prominent landmarks are not clearly visible, and the tracking of clouds is entirely subjective. Many of these difficulties can be overcome through computer processing of digital satellite data. The spin-scan camera on the geostationary satellites has excellent geometric fidelity and the digital data preserve this fidelity. The original brightness resolution is also preserved. Navigation programs can be used to align the data. Objective cloud tracking can be done by using correlation techniques.

An automated cloud-tracking program is used operationally by NOAA/NESS (Green et al., 1975) to perform correlations at preset grid points. Quality control of these data is done by using objective wind field analysis and human editing with the aid of movie loops. This procedure has been successful for low-level cloud motions over the oceans where fair weather cumulus clouds are abundant. The procedure still has difficulties with upper level or multiple-layer clouds, and daily operations currently depend upon the manned movie-loop procedure for determination of these high-level winds.

Identifying tracer clouds is much easier for people than it is for computers. Tracking well-defined clouds and handling data, on the other hand, are what a computer does best. It is this combination of man and machine which is used in the Man-computer Interactive Data Access System (McIDAS) built by the University of Wisconsin (Chatters and Suomi, 1975; Smith, 1975).

With McIDAS the original data are stored on disks under the control of a dedicated computer. The images of the data are displayed on a television screen, from which the operator can select cloud tracers by using a cursor. The computer then fetches the appropriate data from the disk, tracks the cloud by using correlation algorithms, performs some quality control checks on the

data, and then displays the computed wind vector overlaid on the television screen image. The system is flexible and allows completely manual tracking, automatic grid-point tracking, overlays of measurements and contours of surface or radiosonde data, and cloud height measurements, in addition to the basic man-computer interactive tracking. Hence the operator and the computer can work interactively, with the operator making decisions and the computer accessing and processing the data with maximum efficiency. Figure 4.4 shows an operator terminal of McIDAS.

4.4 Space and Time Resolution Requirements

The basic concept behind cloud drift winds is that some clouds are passive tracers of the air's motion in the vicinity of the cloud. However, clouds grow and decay with lifetimes which are related to their size. To qualify for tracking, the tracer cloud's lifetime must be long compared with the interval covered by the tracking sequence (Fujita and Pearl, 1975). The cloud must also be large compared with the resolution of the images. This implies a match between the spatial and temporal resolution of the image sequence. In order for a cloud to be an identifiable feature on an image, it generally must occupy an area at least 10 to 20 pixels across (a pixel is an instantaneous field of view). Hence for full-resolution, 0.8 km SMS/GOES data, the smallest clouds which can be used for tracking are 8-16 km across. Experience has shown that a time interval of approximately 3-10 minutes between images is necessary to track clouds of this size, with the shorter time interval being required for disturbed situations. By averaging pixels together to obtain a coarser resolution, larger clouds can be tracked with longer time intervals between images. Experience has shown that 1.6 km resolution data need 6-15 minute intervals, and 4.8 and 6.4 km resolution data can operate with 30 minute intervals. The normal interval between images for

the SMS/GOES is 30 minutes, though faster scans can be obtained by special request. The operational use of the SMS/GOES data is generally with 3.2-6.4 km resolution images with 30 minute intervals between them. The cloud tracers are therefore at least 32-64 km across and as such represent an average synoptic-scale flow over the volume of air being traced.

4.5 Cloud Heights

Whenever the wind changes with height, the accurate determination of the height of the cloud being tracked is important. There are several ways in which cloud heights can be determined. The operator looking at the visible cloud pictures can guess at cloud heights by identifying the cloud type (for example, cirrus). In the absence of other height data, such as with the ATS images, the operator's assigned height has been shown to be good for two levels--high (cirrus) and low (trade cumulus) clouds.

Another method of determining cloud heights is through the use of stereo projections, from two satellites or from a single polar-orbit satellite looking ahead and behind. The height resolution is limited by the pixel size on the image and the angular base-line displacement between the two satellites. With this method the heights of clouds could be measured to five to ten levels, but the technique has not been attempted yet in conjunction with an operational cloud-tracking system.

Cloud shadows may also be used to measure cloud heights in the same way that the heights of mountains on the moon have been measured. This method is limited by the resolution of the image, the knowledge of the height of the surface beneath the cloud, and the availability of shadows. The method is of limited practical value.

Infrared sounder data offer information on cloud heights. This information is generated routinely as a part of the inversion of polar orbiter

satellite sounder data (Smith and Woolf, 1976), but it has not been applied to any cloud-tracking system. The resolution of this method is about ten levels. When geostationary VAS sounders are available in the 1980's it may be come an operationally feasible method.

Finally, the cloud heights can be determined by the use of the infrared image data (section 3.3.9). This is the method used at the University of Wisconsin and by most other cloud-tracking systems. The infrared cloud temperature is equated with the actual cloud top temperature, and the height is determined through a proximate sounding. The main problem with this method is that clouds are not necessarily blackbody radiators. Some of the energy reaching the sensor may come from lower down in the atmosphere, making the clouds appear warmer than they actually are.

Platt (1975) showed that, while cirrus clouds as a whole have very low emissivity, there are regions of cirrus-generating cells where the emissivity is almost unity. Hubert (1975) of NOAA/NESS used this information to develop a cirrus tracer height technique, which operates as follows. The infrared temperature of these thicker, more emissive regions is colder than the temperature of the surrounding cirrus. The operator measures the temperature of these colder spots, converts it to height by using a sounding, and then assigns this height to all vectors in the vicinity of and with approximately the same speed as the colder cell.

The height assignment of the tracked cloud is probably the largest source of error in cloud-tracked winds at present. In addition to problems of measuring cloud top height, there is the problem of determining where in the atmosphere the source of the momentum which is moving the cloud is. In situ measurements by Hasler, Shenk, and Skillman (1976, 1977) show that a low-level ocean cumulus cloud moves with the velocity of the air at its base and that a

cirrus moves with the mean wind of the cloud layer. Additional information as to what level is appropriate for the height assignment of cloud displacements is still required for the larger cloud systems which are routinely tracked for synoptic-scale flow.

4.6 Accuracy of Cloud Winds

Errors in cloud drift wind measurements can be caused by many factors. These include image alignment errors, image granularity, cloud growth and dissipation, cloud height uncertainties, and cloud motions not associated with winds, such as gravity wave clouds. Alignment errors (which are systematic in nature) generally are quite small (less than 1 m/sec). Image granularity errors random errors associated with uncertain ties of the location of a cloud within a single image pixel. This error is approximately the image pixel size divided by the time between images. Cloud height errors cause wind errors if there is wind shear. Cloud growth and dissipation errors are minimized by selecting cloud tracers which are nearly passive. Fujita and Pearl (1975) estimated the uncertainty of cloud winds due to growth and dissipation within cumulus tracers to be approximately 2 m/sec.

Error analyses can be made by either comparisons with ground truth or by performing a system noise study. Hubert and Thomasell (1979) have performed both types of error analyses to the cloud winds operationally produced by NESS. Their analysis shows low level winds to have an rms vector error of 2.5 m/sec and high level winds to have an rms vector error of 4.0 m/sec. When cloud winds are compared with radiosonde winds, the effects of atmospheric variables due to none coincidence add to those of the basic system noise. Comparisons with radiosondes had rms vector errors of 4.7 m/sec for low level winds and 8.5 m/sec for high level winds.

4.7 Limitation of Cloud Drift Winds

Most of the technical problems associated with obtaining cloud drift winds have been solved. Studies by Bauer (1976), Suchman and Martin (1976), and others have shown that cloud drift winds can be as accurate as radiosonde winds. However, the cloud drift wind techniques are not about to put the radiosondes out of business. The cloud winds are a limited and meteorologically biased data set. While radiosondes obtain wind measurements at many levels, the cloud winds generally yield wind measurements from only one level--the upper-most layer of cloud. Information on cloud motions at different levels is generally obtained from different geographic areas.

Cloud winds also form a data set which is meteorologically biased toward regions where the air is going up (and hence produces the clouds). While this should not cause any problems for synoptic uses of the cloud motion data, it could cause serious interpretation problems for climatology studies. In a general circulation study using only cloud drift winds, Hinton (1977) shows that the Hadley circulation appears to extend into midlatitudes and that the transports are much more vigorous than has been found in other studies which used only radiosonde winds. This is because the cloud winds are biased toward the eddy processes which account for much of the transport. The cloud winds miss many of the weaker return motions which are associated with clear subsiding air.

4.8 Present State and Future of Cloud Drift Winds

Cloud tracked winds are operationally produced by NESS, the European Space Agency, and the Japanese Meteorological Service. With the launch of the Indian geostationary satellite scheduled for the summer of 1983, a global data base of cloud tracked winds will be operationally produced. A preview of this global data base was produced during the First GARP Global Experiment (FGGE)

during the year of 1979. Figures 4.5 and 4.6 show examples of the low and high level cloud tracked winds from 11 January 1979. Except for some additional measurements made in the tropics as part of FGGE, this wind set is fairly representative of the cloud tracked winds operationally produced today.

The cloud wind can also be useful for scales smaller than synoptic. Suchman and Martin (1976) used subsynoptic-scale wind measurements to study cloud clusters in the GARP Atlantic Tropical Experiment region. Houghton and Wilson (1976) measured mesoscale wind fields around a severe storm which produced a tornado and obtained reasonable vertical motions by using convergence of the measured cloud winds. Both NASA and NOAA are currently conducting research programs on obtaining wind fields around hurricanes and tornadoes by using rapid-scan SMS/GOES images with 3-15 minutes between images. The cloud winds can fill in some of the data gaps between radiosonde stations and between radiosonde launch times. Winds produced by tracking water vapor images from meteosat and VAS appear to offer a way of getting wind information in clear regions and mid levels. Hence it appears that in the future, cloud drift winds will be useful over data-sparse regions of the globe for long-range synoptic forecasts and over data-sparse subsynoptic and mesoscale regions for short-range severe storm forecasts.

References

Anding, D. and R. Kauth, 1970: Estimation of Sea Surface Temperature from Space. Remote Sensing of the Environment, 1, 217-220.

Barnett, T. P., W. C. Patzert, S. C. Webb, and B. R. Bean, 1979: Climatological Usefulness of Satellite Determined Sea-Surface Temperatures in the Tropical Pacific. Bulletin of the American Meteorological Society, 60, 197-205.

Bates, J. J., 1982: Sea surface temperatures derived from VAS multispectral data. M.S. thesis, Department of Meteorology, University of Wisconsin, Madison, Wisconsin, 53706, 40 pp.

Bauer, K. T., 1976: A comparison of cloud motion winds with coinciding radiosonde winds. Monthly Weather Review, 104, 922-931.

Bengtsson, L., 1981: The impact of FGGE on global medium range forecasts. Characteristics of atmospheric planetary circulations and associated model forecast skill during FGGE case studies selected by WGNE. In Proceedings of the International Conference on Early Results of FGGE and Large-Scale Aspects of its Monsoon Experiments, Tallahassee, Florida, 12-17 January 1981.

Biglow, F. H., 1904: The average monthly vectors of the general circulation in the United States. Monthly Weather Review, 32, 260.

Browell, E. V., A. F. Carter, and T. I. Wilkerson, 1981: Airborne differential absorption lidar system for water vapor investigations. Optical Engineering, 20, 84-90.

Browell, E. V., 1982: Lidar measurements of tropospheric gases. Optical Engineering, 21, 128-132.

Browell, E. V., A. F. Carter, S. T. Schippley, R. J. Allen, C. F. Butler, M. N. Mayo, J. H. Siveter, Jr., and W. M. Hall, 1983: NASA Multi-purpose airborne dial system and measurements of ozone and aerosol profiles. Applied Optics, 22.

Brower, R. L., H. S. Gohrband, W. G. Pichel, T. L. Signore, and C. C. Walton, 1976: Satellite derived sea surface temperatures from NOAA spacecraft. U.S. Department of Commerce, National Oceanic and Atmospheric Administration, National Environmental Satellite Service, Washington, D.C., NOAA Technical Memorandum NESS 78, 74 pp.

Chahine, M. T., 1968: Determination of the temperature profile in an atmosphere from its outgoing radiance. Journal of the Optical Society of America, 58, 1634.

Chahine, M. T., 1970: A general relaxation method for inverse solution of the full radiative transfer equation. Journal of Atmospheric Science, 27, 960.

Chahine, M. T., 1974: Remote sounding of cloudy atmospheres, 1. The single cloud layer. Journal of Atmospheric Science, 31, 233-243.

Chatters, G. C., and V. E. Suomi, 1975: The applications of McIDAS. IEEE Trans. Geosci. Electron., GE-13, 137-146.

Conrath, B. J., 1969: On the estimation of relative humidity profiles from medium resolution infrared spectra obtained from a satellite. Journal of Geophysical Research, 74, 3347-3361.

Crosby, D. S., and K. S. Glasser, 1978: Radiance estimates from truncated observations. Journal of Applied Meteorology, 17, 1712-1715.

Douglas, C. K. M., 1922: Observations of upper cloud drift as an aid to research and to weather forecasting. Quarterly Journal of the Royal Meteorological Society, 48, 342-356.

Fleming, H. E., and W. L. Smith, 1971: Inversion techniques for remote sensing of atmospheric temperature profiles. Reprint from Fifth Symposium on Temperature, Instrument Socieity of America, 400 Stanwix Street, Pittsburgh, Pennsylvania, 2239-2250.

Fleming, H. E., and L. M. McMillin, 1977: Atmospheric transmittance of an absorbing gas 2: a computationally fast and accurate transmittance model for slant paths at different zenith angles. Applied Optics, 16, 1366-1370.

Foster, M., 1961: An application of Wiener-Kolmogorov smoothing theory to matrix inversion. Journal of the Society for Industrial and Applied Mathematics, 9, 387-392.

Fritz, S., D. Q. Wark, H. E. Fleming, W. L. Smith, H. Jacobowitz, D. T. Hilleary, and J. C. Alishouse, 1972: Temperature sounding from satellites. U.S. Department of Commerce, National Oceanic and Atmospheric Administration, National Environmental Satellite Service, Washington, D.C., NOAA Technical Report NESS 59, 49 pp.

Fujita, T. T., and E. W. Pearl, 1975: Satellite tracked cumulus velocities. Journal of Applied Meteorology, 14, 407-413.

Gill, R., K. Geller, J. Farine, J. Cooney and A. Cohen, 1979: Measurement of atmospheric temperature profiles using Raman lidar. Journal of Applied Meteorology, 18, 225-227.

Gille, J. C., 1979: Middle atmosphere processes revealed by satellite observations. Journal of Atmospheric and Terrestrial Physics, 41, 707-722.

Greaves, J. R., G. DiMego, W. L. Smith, and V. E. Suomi, 1979: A special effort to provide improved sounding and cloud motion wind data for FGGE. Bulletin of the American Meteorological Society, 60, 124-127.

Green, R., G. Hughes, C. Novak, and R. Schreitz, 1975: The automatic extraction of wind estimates from VISSR data. In Central Processing and Analysis of Geostationary Satellite Data, NOAA Technical Memorandum NESS 64, 94-110.

Grody, N. G., A. Gruber, and W. Shen, 1980: Atmospheric water content over the tropical Pacific derived from the Nimbus-6 scanning microwave spectrometer. Journal of Applied Meteorology, 19, 986-996.

Hambrick, L. N., and D. R. Phillips, 1980: Earth locating image data of spin-stabilized geostationary satellites. NOAA Technical Memorandum NESS 111.

Hasler, A. F., W. E. Shenk, and W. C. Skillman, 1976: Wind estimates from cloud motions: Phase 1 of an in situ aircraft verification experiment. Journal of Applied Meteorology, 15, 10-15.

Hasler, A. F., W. E. Shenk, and W. C. Skillman, 1977: Wind estimates from cloud motions: Results of phases I, II and III of an in situ aircraft verification experiment. Journal of Applied Meteorology, 16, 812-815.

Hayden, C. M., W. L. Smith, and H. M. Woolf, 1981: Determination of moisture from NOAA polar orbiting satellite sounding radiances. Journal of Applied Meteorology, 20, 450-466.

Hinton, B. B., 1977: Climatology based on winds derived from cloud motions. In Studies of Soundings and Imaging Measurements, Final Scientific Report on NAS5-21798, Space Science and Engineering Center, University of Wisconsin, Madison, 231-273.

Houghton, D. D., and T. A. Wilson, 1976: Mesoscale wind fields for a severe storm situation determined from synchronous meteorological satellite (SMS) cloud observations. In Proc. Ninth Conference on Severe Local Storms, Norman, Oklahoma; American Meteorological Society, Boston, Massachusetts, 187-192.

Houghton, J. T., 1978: The stratosphere and mesosphere. Quarterly Journal of the Royal Meteorological Society, 104, 1-29.

Hubert, L. F., 1975: Note on jet cirrus emissivity. Quarterly Journal of the Royal Meteorological Society, 101, 1017-1019.

Hunt, G. E., 1973: Radiative properties of terrestrial clouds at visible and infrared thermal window wavelengths. Quarterly Journal of the Royal Meteorological Society, 99, 346-369.

Kaplan, L. D., 1959: Inference of atmospheric structure from remote radiation measurements. Journal of the Optical Society of America, 49, 1004.

Kaplan, L. D., M. T. Chahine, J. Susskind, and J. E. Searl, 1977: Spectral band passes for a high precision satellite sounder. Applied Optics, 16, 322-325.

King, J. I. F., 1956: The radiative heat transfer of planet earth. In Scientific Use of Earth Satellites, University of Michigan Press, Ann Arbor, Michigan, pp. 133-136.

Korb, C. L., and C. Y. Weng, 1982: A theoretical study of a two-wavelength lidar technique for the measurement of atmospheric temperature profiles. Journal of Applied Meteorology, 21, 1346-1355.

Lauritson, L., G. J. Nelson, and F. W. Porto, 1979: Data extraction and calibration of TIROS-N/NOAA radiometers. U.S. Department of Commerce, National Oceanic and Atmospheric Administration, National Earth Satellite Service, Washington, D.C., NOAA Technical Memorandum NESS 107, 73 pp.

Marvin, C. F., 1896: Cloud observations and an improved nephosocpe. Monthly Weather Review, 24, 9-13.

Mason, J. B., 1975: Lidar measurement of temperature: A new approach. Applied Optics, 14, 76-78.

McClain, E. P., W. Pichel, C. Walton, A. Ahmad, and J. Sutton, 1982: Multichannel improvements to satellite-derived global sea surface temperatures. Preprint, XXIV COSPAR, Ottawa, Canada, 22-29 May 1982.

McMillin, L. M., D. Q. Wark, J. M. Siomkajlo, P. G. Abel, A. Werbowetzki, L. A. Lauritson, J. A. Pritchard, D. S. Crosby, H. M. Woolf, R. C. Luebbe, M. P. Weinreb, H. E. Fleming, F. E. Bittner, and C. M. Hayden, 1973: Satellite infrared soundings from NOAA Spacecraft. U.S. Department of Commerce, National Oceanic and Atmospheric Administration, National Environmental Satellite Service, Washington, D.C., NOAA Technical Report NESS 65, 112 pp.

McMillin, L. M., and H. E. Fleming, 1976: Atmospheric transmittance of an absorbing gas: a computationally fast and accurate transmittance model for absorbing gases with constant mixing ratios in homogeneous atmospheres. Applied Optics, 15, 358.

McMillin, L. M., and C. Dean, 1982: Evaluation of a new operational technique for producing clear radiances. Journal of Applied Meteorology, 12, 1005-1014.

Menzel, W. P., W. L. Smith, and T. Stewart, 1983: Improved cloud motion wind vector and altitude assignment using VAS. Journal of Applied Meteorology, (February issue).

Mosher, F. R., 1978: Cloud drift winds from geostationary satellites. Atmospheric Technology, 10, 53-60.

Pick, W. H., and D. F. Bowering, 1929: Cirrus movement and the advance of depressions. Quarterly Journal of the Royal Meteorological Society, 55, 71-112.

Platt, C. M. R., 1975: Infrared emissivity of cirrus-simultaneous satellite, lidar and radiometric observations. Quarterly Journal of the Royal Meteorological Society, 101, 119-126.

Prabhakara, C., G. Dalu, and V. G. Kunde, 1974: Estimation of sea surface temperature from remote sensing in the 11 to 13 μm window region. Journal of Geophysical Research, 79, 5039-5044.

Rodgers, C. D., 1970: Remote sounding of the atmospheric temeprature profile in the presence of cloud. Quarterly Journal of the Royal Meteorological Society, 11, 767.

Rodgers, C. D., 1976: Retrieval of atmospheric temperature and composition from remote measurements of thermal radiation. Rev. of Geophysics and Space Physics, 14, 609-624.

Rosenkranz, P. W., M. J. Komichak, and D. H. Staelin, 1982: A method for estimation of atmospheric water vapor profiles by microwave radiometry. Journal of Applied Meteorology, 21, 1364-1370.

Schmidt, H. L., 1982: Program Development Plan for improving weather services through more effective use of GOES remote sensing, September 1982. Copies available from H. L. Schmidt, S/SD1, NOAA/NESDIS Advanced Systems Concept Group, FB-4, Room 3010, Washington, D.C., 20233.

Smith, E. A., 1975: The McIDAS system. IEEE Trans. Geosci. Electron., GE-13, 123-136.

Smith, W. L., 1968: An improved method for calculating tropospheric temperature and moisture from satellite radiometer measurements. Monthly Weather Review, 96, 387.

Smith, W. L., 1970: Iterative solution of the radiative transfer equation for temperature and absorbing gas profiles of an atmosphere. Applied Optics, 9, 1993-1999.

Smith, W. L., P. K. Rao, R. Koffler, and W. R. Curtis, 1970: The determination of sea surface temperature from satellite high-resolution infrared window radiation measurements. Monthly Weather Review, 98, 604-611.

Smith, W. L., H. M. Woolf, and W. J. Jacob, 1970: A regression method for obtaining real-time temperature and geopotential height profiles from satellite spectrometer measurements and its application to Nimbus-3 SIRS observations. Monthly Weather Review, 98, 582-603.

Smith, W. L., and H. B. Howell, 1971: Vertical distribution of atmospheric water vapor from satellite infrared spectrometer measurements. Journal of Applied Meteorology, 10, 1026.

Smith, W. L., H. M. Woolf, and H. E. Fleming, 1972: Retrieval of atmospheric temperature profiles from satellite measurements for dynamical forecasting. Journal of Applied Meteorology, 11, 113.

Smith, W. L., H. M. Woolf, P. G. Abel, C. M. Hayden, M. Chalfant, and N. Grody, 1974: Nimbus-5 sounder data processing system part I: measurement characteristics and data reduction procedures. Final report for GARP Project Office, NASA Contract S-70249-AG, NOAA Technical Memorandum NESS 57, 99 pp., (Available from NTIS, Springfield, Virginia).

Smith, W. L., P. G. Abel, H. M. Woolf, H. W. McCulloch, and B. J. Johnson, 1975: The High-resolution Infrared Radiation Sounder (HIRS) experiment. Nimbus-6 User's Guide, Goddard Space Flight Center, Greenbelt, Maryland, 20771.

Smith, W. L., and H. M. Woolf, 1976: The use of eigenvectors of statistical covariance matrices for interpreting satellite sounding radiometer observations. Journal of Atmospheric Science, 35(7), 1127-1140.

Smith, W. L., J. R. Hickey, H. B. Howell, H. Jacobowitz, D. T. Hilleary, and A. J. Drummond, 1977: Nimbus-6 earth radiation budget experiment. Applied Optics, 16, 306-318.

Smith, W. L., and C. M. R. Platt, 1977: A laser method of observing surface pressure and pressure-altitude and temperature profiles of the troposphere from satellites. U.S. Department of Commerce, National Oceanic and Atmospheric Administration, National Environmental Satellite Service, Washington, D.C., NOAA Technical Memorandum NESS 89, 38 pp.

Smith, W. L., C. M. Hayden, H. M. Woolf, H. B. Howell, and F. W. Nagle, 1978: Interactive processing of TIROS-N sounding data. Preprints, Conference on Weather Forecasting and Analysis and Aviation Meteorology (Silver Spring, Maryland), American Meteorological Society, Boston, pp. 390-395.

Smith, W. L., H. M. Woolf, C. M. Hayden, D. Q. Wark, and L. M. McMillin, 1979: The TIROS-N operational vertical sounder. Bulletin of the American Meteorological Society, 60, 1177-1187.

Smith, W. L., H. B. Howell, and H. M. Woolf, 1979: The use of interferometric radiance measurements for sounding the atmosphere. Journal of Atmospheric Science, 36, 566-575.

Smith, W. L., 1980: Sea surface temperature: improved observation from geostationary satellites. Proceedings of a Workshop on Applications of Existing Satellite Data to the Study of Ocean Surface Energetics, University of Wisconsin, Madison, Wisconsin, 53706, 19-21 November 1980, pp. 163-168.

Smith, W. L., V. E. Suomi, W. P. Menzel, H. M. Woolf, L. A. Sromovsky, H. E. Revercomb, C. M. Hayden, D. N. Erickson, and F. R. Mosher, 1981: First sounding results from VAS-D. Bulletin of the American Meteorology Society, 62, 232-236.

Smith, W. L., 1981: Proposal submitted to National Aeronautics and Space Administration, "High Resolution Interferometer Sounder (HIS) Phase II." Available from Space Science and Engineering Center, 1225 West Dayton Street, Madison, Wisconsin, 53706.

Smith, W. L., and F. X. Zhou, 1982: Rapid extraction of layer relative humidity, geopotential thickness, and atmospheric stablity from satellite sounding radiometer data. Applied Optics, 21, 924-928.

Smith, W. L., 1983: The retrieval of atmospheric profiles from VAS geostationary radiance observations. Journal of Atmospheric Science, 40, 2025-2035.

Staelin, D. H., K. F. Kunzi, R. L. Pettyjohn, R. K. L. Poon, R. W. Wilcox, and J. W. Waters, 1976: Remote sensing of atmospheric water vapor and liquid water with the Nimbus-5 microwave spectrometer. Journal of Applied Meteorology, 15, 1204-1214.

Strand, O. N., and E. R. Westwater, 1968: Statistical estimation of the numerical solution of a Fredholm integral equation of the first kind. J. Ass. Comput. Mach., 15, 100.

Suchman, D., and D. W. Martin, 1976: Wind sets from SMS images: An assessment of quality for GATE. Journal of Applied Meteorology, 15, 1265-1278.

Suomi, V. E., R. Fox, S. S. Limaye, and W. L. Smith, 1982: McIDAS III: A modern interactive data access and analysis system. Accepted for publication in May 1983 Journal of Climate and Applied Meteorology.

Tikhonov, A. N., 1963: On the solution of incorrectly states problems and a method of regularization. Dokl. Acad. Nauk SSSR, 151, 501.

Turchin, V. F., and V. Z. Nozik, 1969: Statistical regularization of the solution of incorrectly posed problems, Izv. Acad. Sci. USSR Atmos. Oceanic Phys., 5, 14.

Twomey, S., 1963: On the numerical solution of Fredholm integral equations of the first kind by the inversion of the linear system produced by quadrature. J. Ass. Comput. Mach., 10, 97.

Twomey, S., 1965: The application of numerical filtering to the solution of integral equations encountered in indirect sensing measurements. J. Franklin Inst., 279, 95.

Twomey, S., 1977: An introduction to the mathematics of inversion in remote sensing and indirect measurements. Elsevier, New York.

Uccellini, L. W., and D. R. Johnson, 1979: The coupling of upper and lower tropospheric jet streaks and implications for the development of severe convective storms. Monthly Weather Review, 107, 682-703.

Walton, C. C., R. L. Brower, and T. L. Signore, 1976: Satellite-derived sea surface temperatures by multi-channel regression. Proceedings of COSPAR Symposium on Meteorological Observations from Space, COSPAR XIX, Philadelphia, Pennsylvania, 8-10 June 1976, 155-159.

Walton, C., 1980: Deriving sea surface temperatures from TIROS-N data. Remote Sensing of Atmospheres and Oceans, Academic Press, 547-579.

Wark, D. Q., 1961: On indirect temperature soundings of the stratosphere from satellites. Journal of Geophysical Research, 66, 77.

Wark, D. Q., and H. E. Fleming, 1966: Indirect measurements of atmospheric temperature profiles from satellites, 1. Introduction. Monthly Weather Review, 94, 351.

Wilheit, T. T., and A. T. C. Chang, 1979: An algorithm for retrieval of ocean surface and atmospheric parameters from the observations of the scanning multichannel microwave radiometer (SMMR). NASA Technical Memorandum 80277, National Aeronautics and Space Administration, Goddard Space Flight Center, Greenbelt, Maryland, 20771, 30 pp.

Young, J. T., 1976: Navigation of geostationary images. In Proc. Symposium on Meteorological Observations from Space: Their Contributions to the First GARP Global Experiment, Philadelphia, Pennsylvania. COSPAR Working Group 6, NCAR, Boulder, Colorado, 198-200.

Young, M. T., 1975: The GOES wind operations. In Central Processing and Analysis of Geostationary Satellite Data, NOAA Technical Memorandum NESS 64, 111-121.

TABLE 1.1
REGIONS AND UNITS OF THE ELECTROMAGNETIC SPECTRUM

	WAVELENGTH (λ)			FREQUENCY (f) (cycles/sec)		WAVENUMBER (ν)
	cm	μm (microns)	Å	Hz	GHz	cm^{-1}
NEAR ULTRAVIOLET (UV)	10^{-5}	0.1	1000	$3x10^{15}$		
VISIBLE	$4x10^{-5}$	0.4	4000	$7.5x10^{14}$		
NEAR INFRARED (IR)	$7.5x10^{-5}$	0.75	7500	$4x10^{14}$		13,333
FAR INFRARED (IR)	$2x10^{-3}$	20	200,000	$1.5x10^{13}$		500
MICROWAVE (MW)	0.1	mm/1		$3x10^{11}$	300	10
	10	100		$3x10^{9}$	3	0.1

TABLE 1.2
ATMOSPHERIC ABSORBERS AND THEIR ABSORBING REGIONS

ABSORBER	SYMBOL	SPECTRAL REGION
CARBON DIOXIDE	CO_2	13.5-16.5 μm (center at 15 μm), 4.2-4.4 μm (center at 4.3 μm), 10.4, 9.4, 5.2, 2.7, 2.0, 1.6, and 1.4 μm, also a series of weak bands in the range 0.78-1.24 μm.
MOLECULAR OXYGEN	O_2	1.07 and 1.27 μm, a series of lines between 50-70 GHz, one line at 118.75 GHz, also weak bands in the visible with centers between 5384 and 7621 Å.
WATER VAPOR	H_2O	5.5-7.5 μm (center at 6.3 μm), 2.6-3.3 μm (several centers), 1.9, 1.4, 1.1, 0.94, 0.81, 0.72 μm, 22.24 and 183.31 GHz, plus lines at frequencies higher than 300 GHz that extend all the way to 8 μm, a few weak bands in the visible.
OZONE	O_3	14.1, 9.6, 9.0, 5.75, 4.75, 3.59, 3.27, 2.7 μm, 18 lines between 9.2 and 43.65 GHz, lines at 96.23, 101.74 and 118.36 GHz, plus 20 lines between 160 and 380 GHz. Also 1800-3400 Å (center at 2600 Å), 3200-3600 Å, 4400-7400 Å.
METHANE	CH_4	3.3 and 7.7 μm
NITROUS OXIDE	N_2O	4.5, 7.8, 17.0 μm, plus 251, 75, 50, 25 GHz.
CARBON MONOXIDE	CO	4.67, 2.35, 1.57, 1.19 μm, 2.38-25.0 μm (several centers), plus 230.77 and 115.27 GHz.
WINDOWS	-	8-13 μm, 18, 4.7, 4.0, 3.8, 2.3, 1.65, 1.25, 1.05 μm, regions of the interval 1.4-10.0 GHz, 33-36 GHz, 80-100 GHz, 125-140 GHz, 210-235 GHz, plus the visible region.

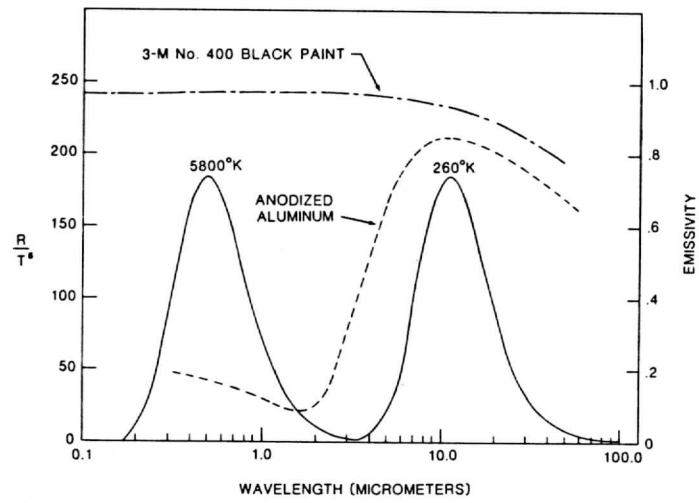

Fig. 1.1: Planck radiance, scaled by temperature to the fifth power, corresponding to the emitting temperature of the sun and the earth-atmosphere system. Also shown is the spectral distribution of the black and aluminum surface coatings used in Suomi's radiation budget radiometer.

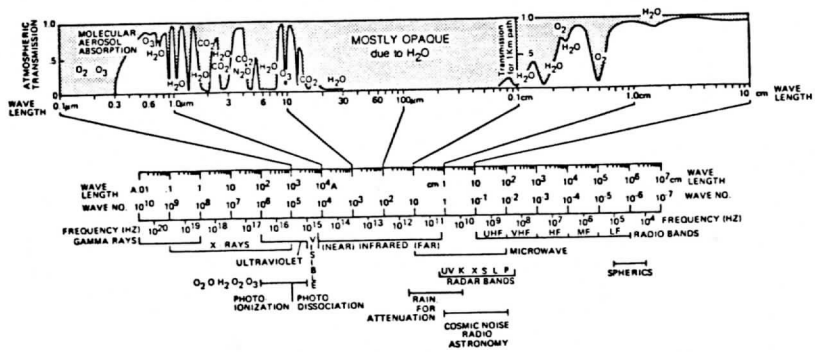

Fig. 1.2: Atmospheric transmission as a function wavelength. The major absorbing constituents are noted.

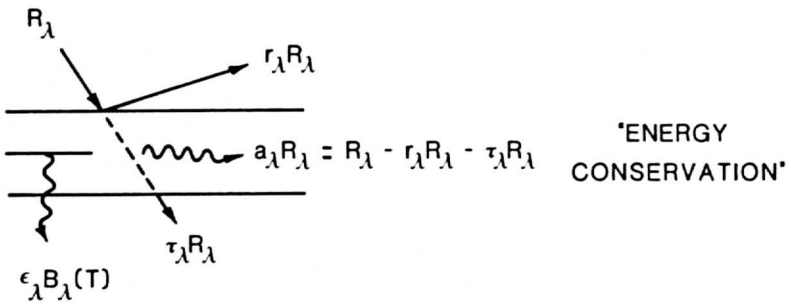

Fig. 1.3: Schematic of radiant energy transfer processes and conservation.

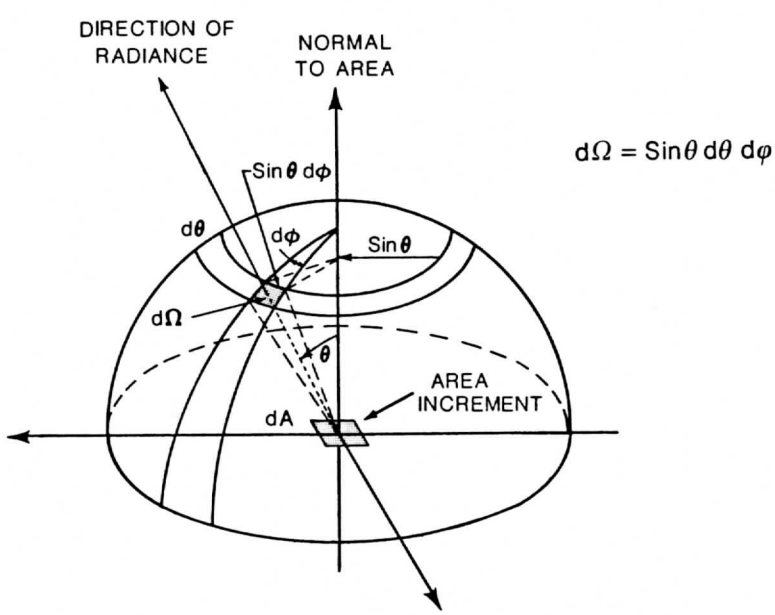

Fig. 1.4: Radiance geometry defining the term solid angle.

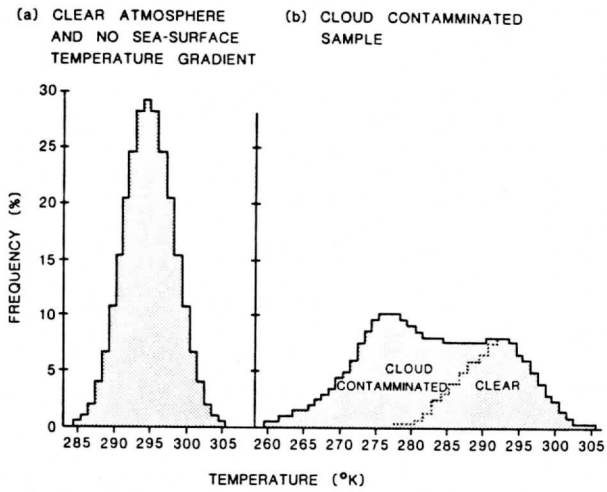

Fig. 2.1: Histogram of infrared window brightness temperature observations; (a) clear atmosphere, and (b) cloudy atmosphere.

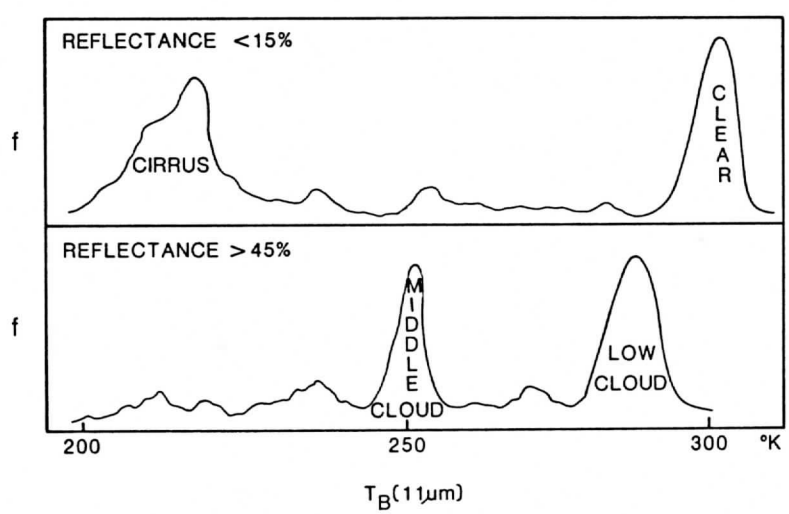

Fig. 2.2: Histograms of infrared brightness temperatures for two visible channel reflectance categories; (a) reflectance less than 15%, and (b) reflectance greater than 45%.

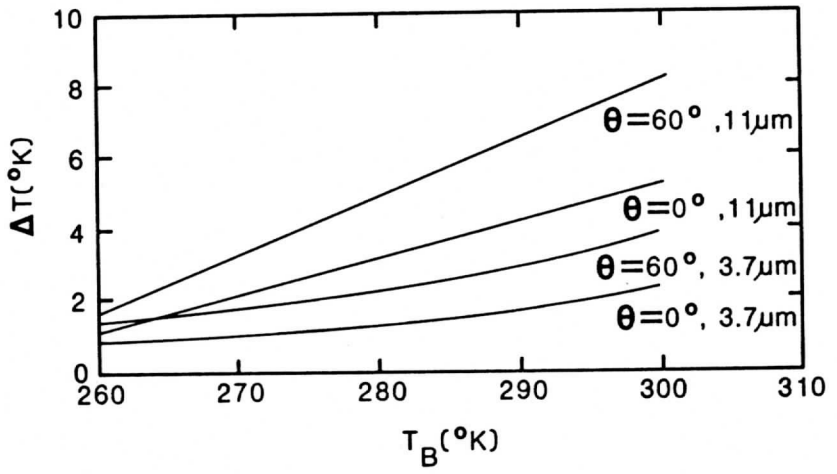

Fig. 2.3: Statistical relations between the water vapor correction as a function of observed brightness temperature for two spectral channels and two viewing angles.

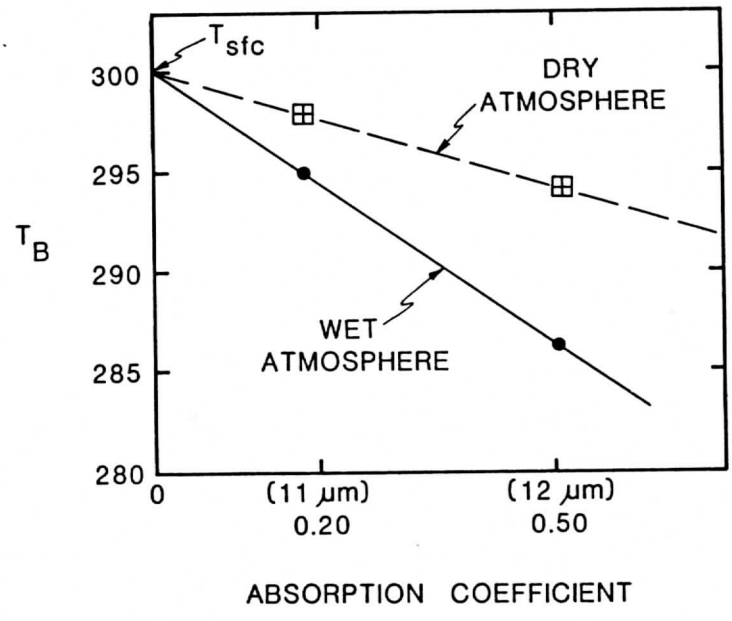

Fig. 2.4: Graphical representation of the linear relation between water vapor attenuation and brightness temperature for two different atmospheric conditions.

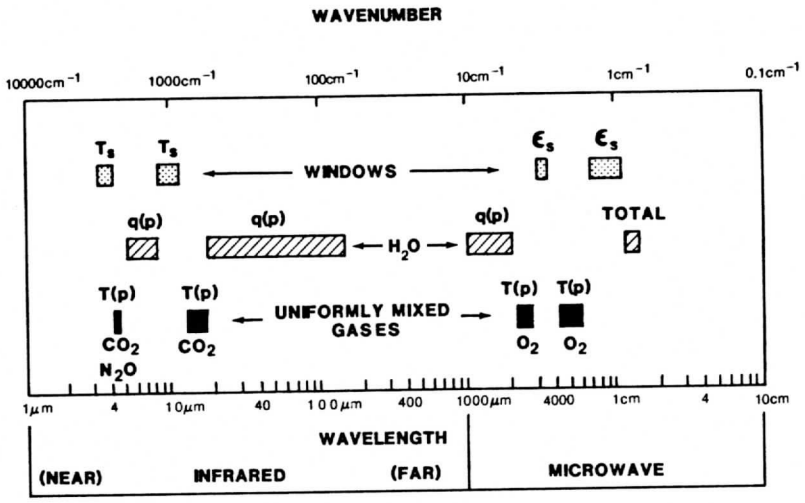

Fig. 3.1: Spectral regions considered useful for remote sensing of surface and atmospheric variables from satellites.

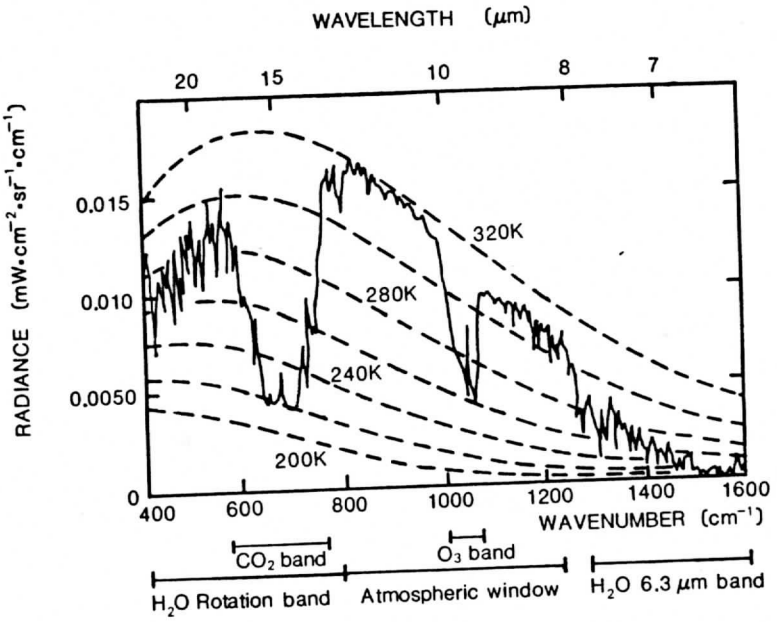

Fig. 3.2: A spectrum of radiance to space observed by the Nimbus-4 IRIS interferometer. The dashed curves are the Planck function for the temperatures indicated.

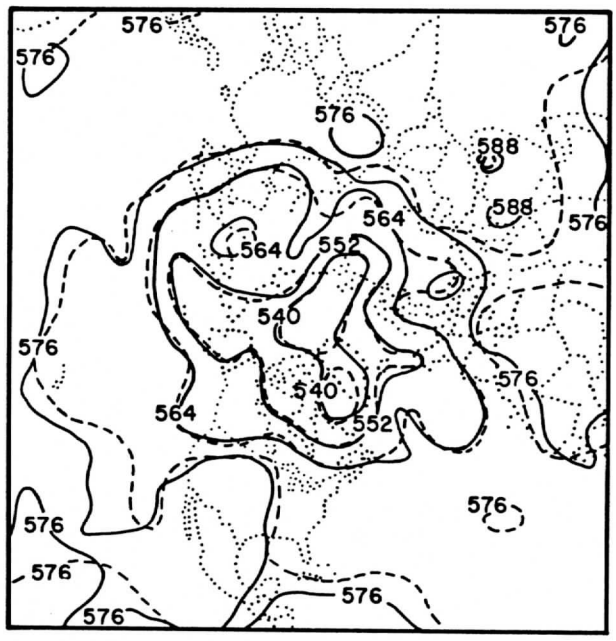

Fig. 3.3: Planck radiance weighting functions for the SIRS-A spectrometer flown on the Nimbus-III satellite. The vertical coordinate is $p^{2/7}$.

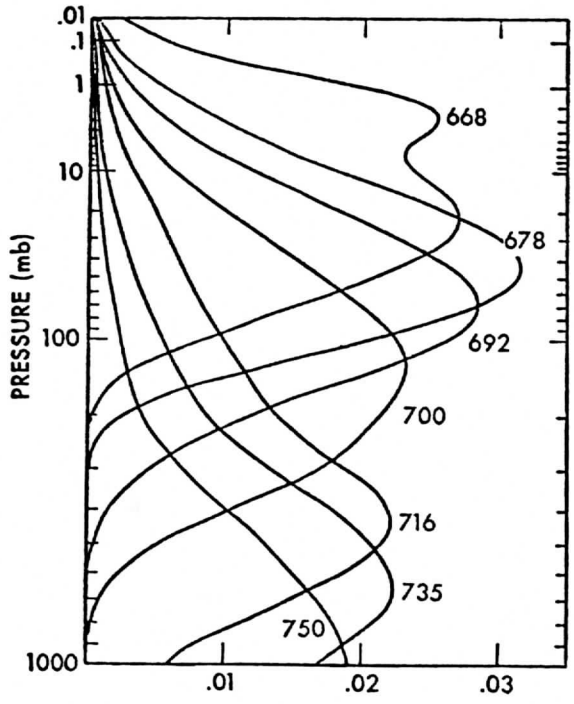

Fig. 3.4: Comparison of an analysis of satellite derived 1000-500 mb thickness values (solid contours) with an independent analysis produced operationally by the National Meteorological Center (dashed contours).

Fig. 3.5: Images of (a) visible and infrared radiance to space in which the light areas correspond to bright cold clouds, (b) water vapor emission in which the light areas correspond to high upper tropospheric water vapor concentrations, and (c) water vapor emission over the mid-United States in which contour analysis of VAS derived 300 mb dewpoint values is shown and radiosonde observations of 300 mb dewpoint (the circled values) are plotted.

3.5(a)

3.5(b)

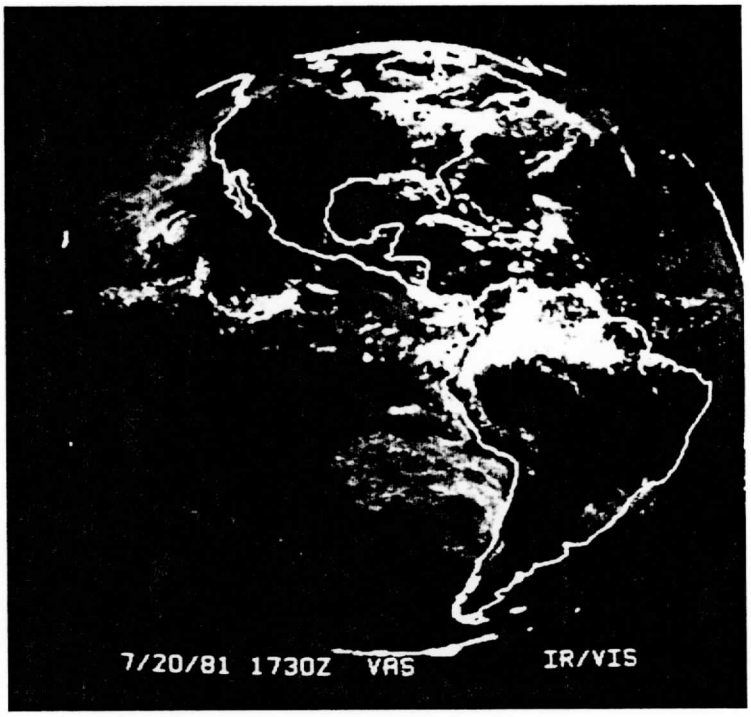

3.5(c)

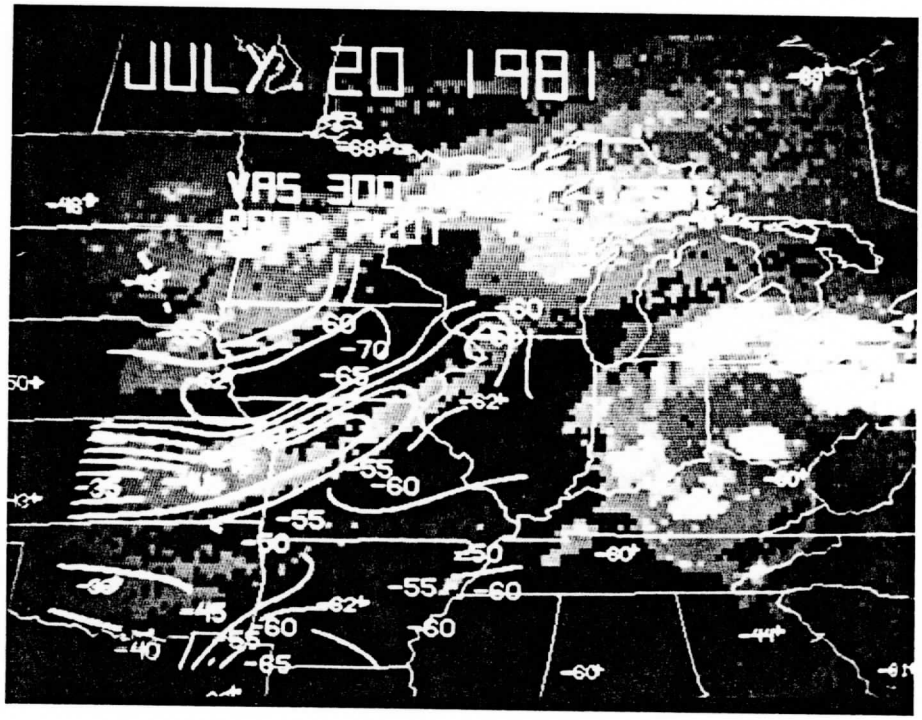

Fig. 3.6: (a) An image of 6.7 μm upper tropospheric water vapor with isolines of total precipitable water (solid contours) and isolines of 300 mb gradient wind speed (dashed lines) superimposed . Contours of the total-totals index derived from VAS soundings superimposed on the cloud imagery for (b) 1500 GMT, (c) 1700 GMT, and (d) 2000 GMT.

3.6(a)

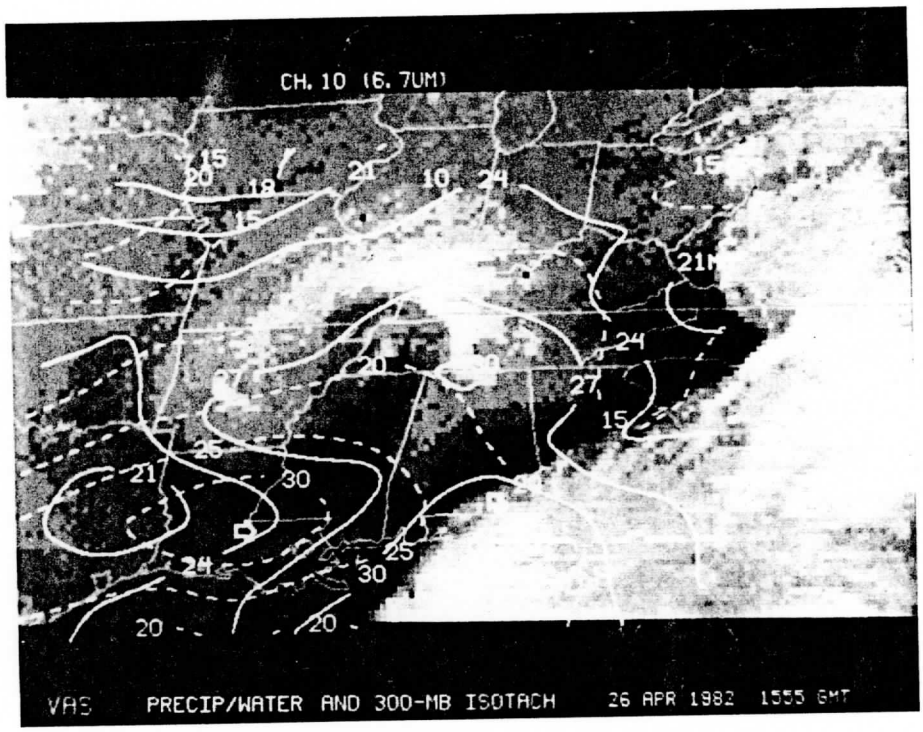

3.6(b)

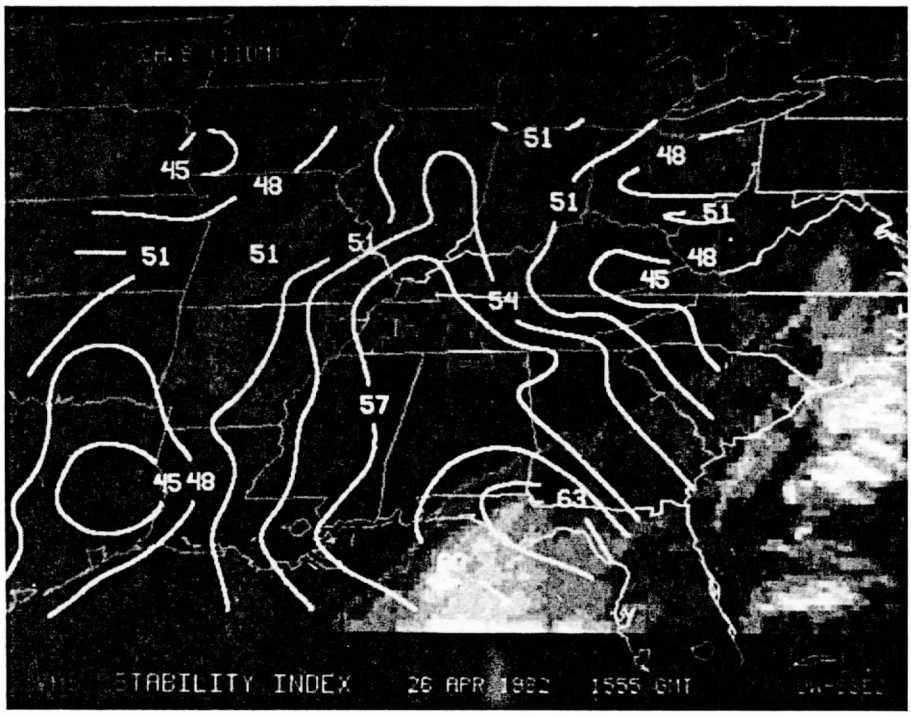

3.6(c)

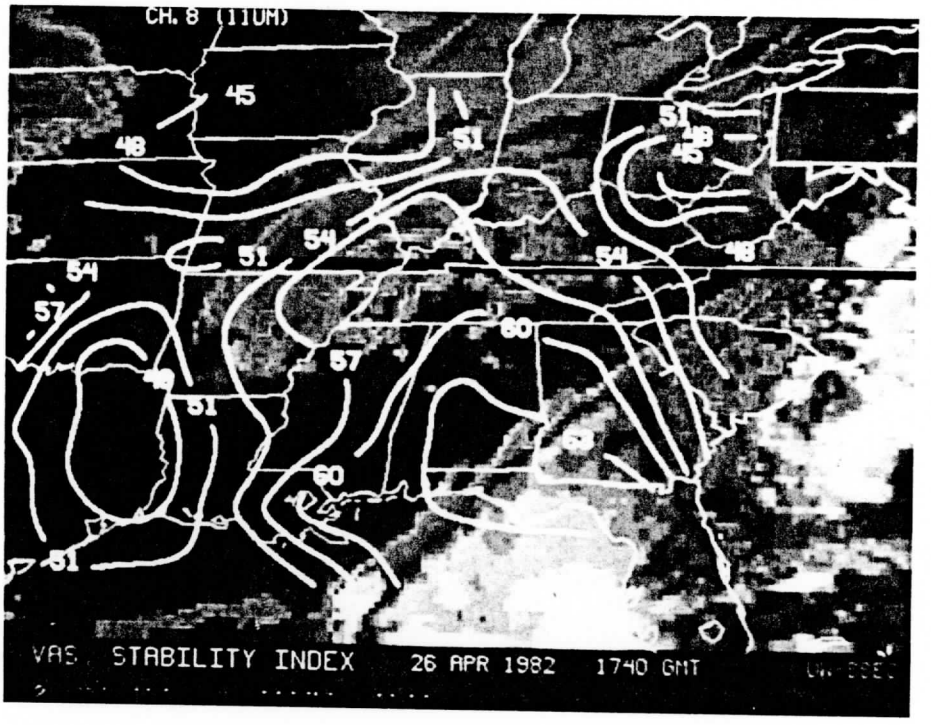
CH. 8 (11UM)
45
48
51
54
57
60
VAS STABILITY INDEX 26 APR 1982 1740 GMT

3.6(d)

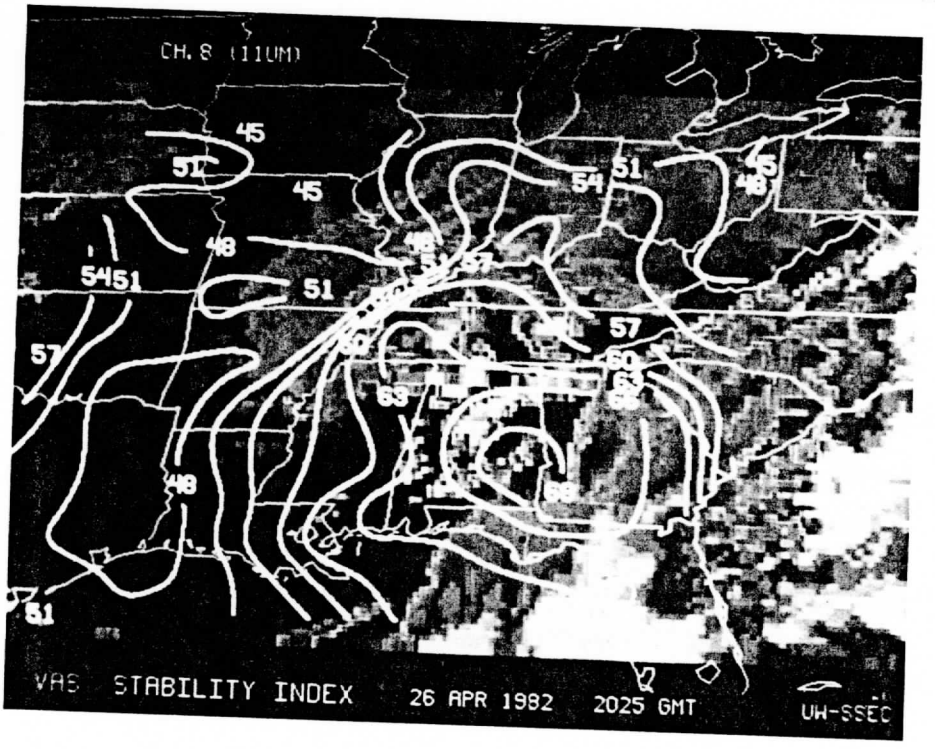
CH. 8 (11UM)
45
48
51
54
57
60
VAS STABILITY INDEX 26 APR 1982 2025 GMT
UW-SSEC

Fig. 3.7: (a) Geometry for a limb viewing satellite-borned radiometer. (b) Weighting functions for a limb-sounding 15 μm broad band radiometer.

3.7(a)

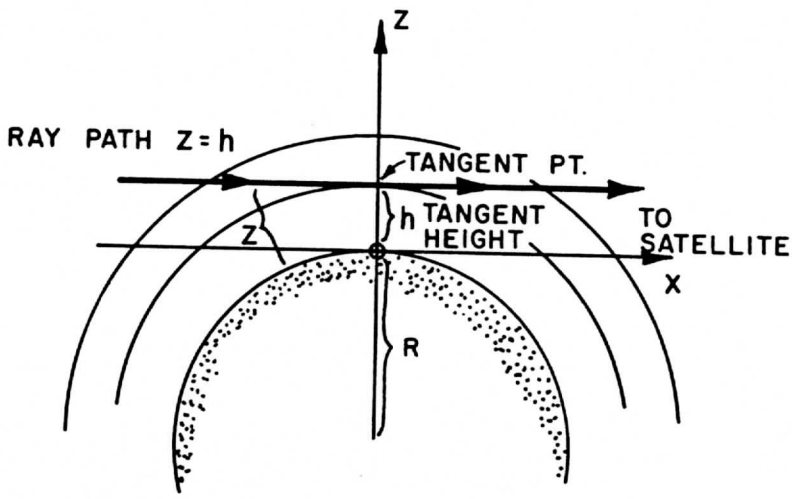

3.7(b)

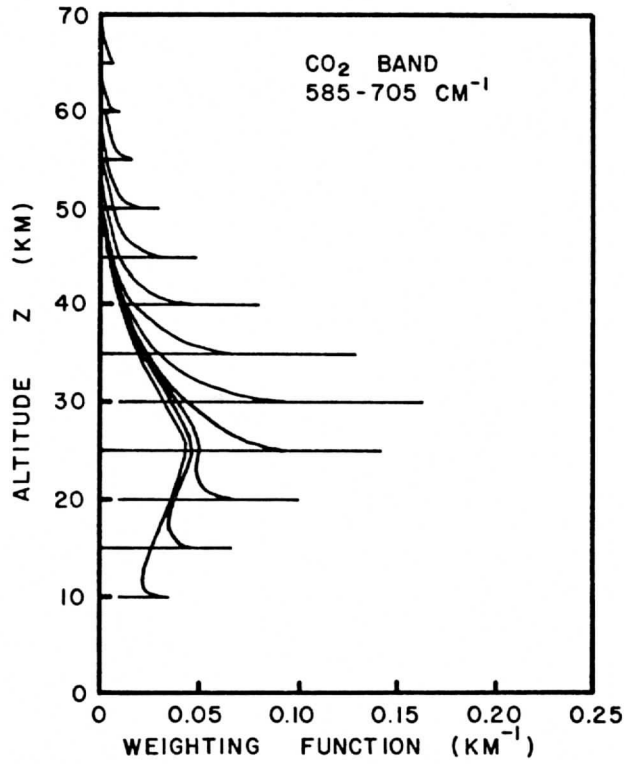

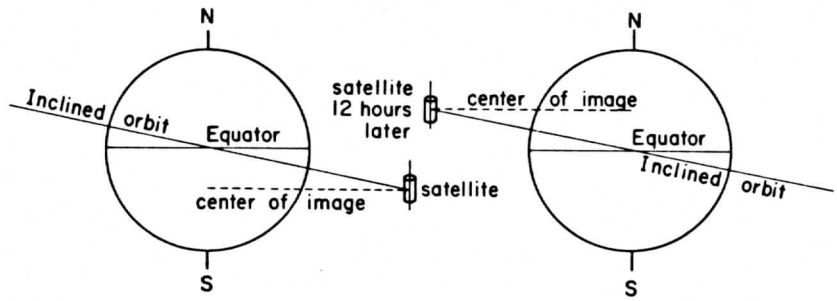

Fig. 4.1: The effect of an imperfect geostationary orbit in causing apparent north-south image motions. The spin axis of the satellite is fixed in space and the image plane is perpendicular to this spin axis. If the orbit is inclined relative to the equator, the satellite will move north and south over the equator daily, causing the image to move north and then south during the day.

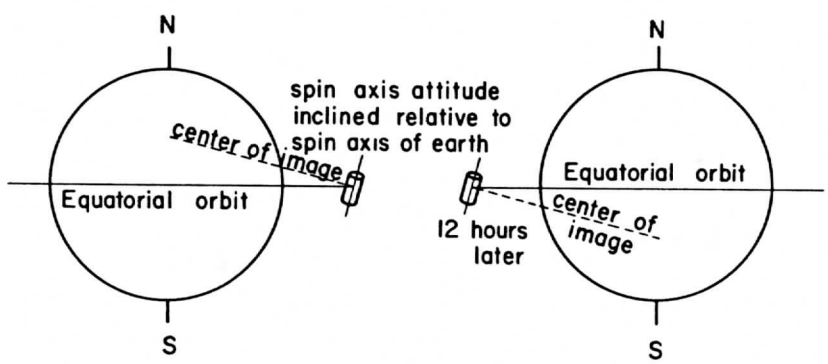

Fig. 4.2: The effect of an imperfect satellite spin axis orientation in causing apparent north-south image motions. If the spin axis of the satellite is not perfectly parallel to the spin axis of the earth, a daily north-south motion will result. At 6 hours from this diagram, the image will be moving back and forth.

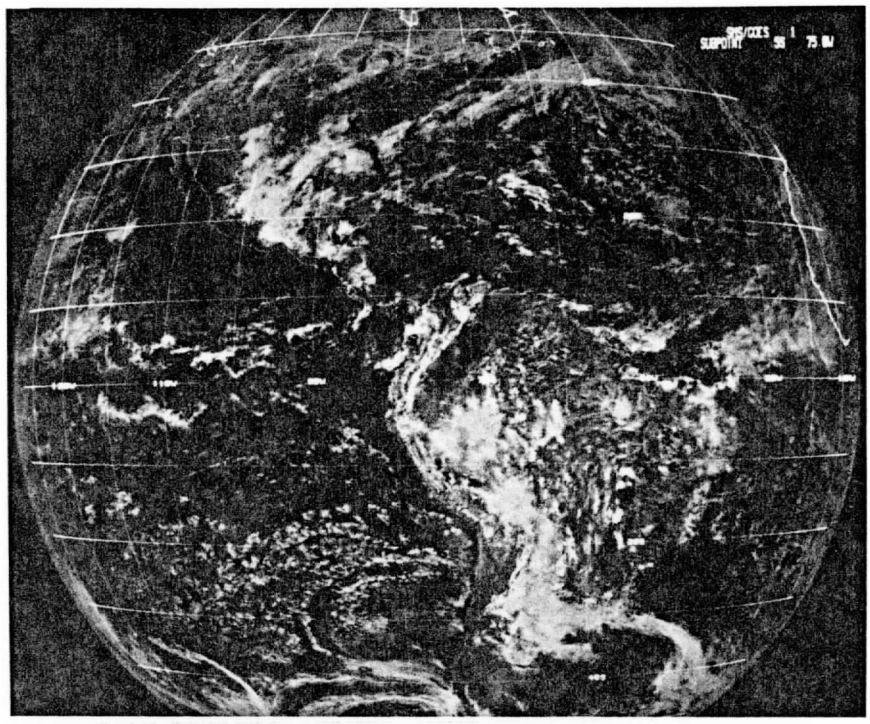

Fig. 4.3: ATS-3 image of the earth on 14 February 1981 at 1700 GMT. The large volume of satellite image data was originally stored on photographic film. Access to the data was easy (just look at the picture), yet quantitative measurements were difficult.

Fig. 4.4: Operator terminal of the Man-computer Interactive Data Access System (McIDAS). The digital data are stored on disks under computer control. The operator identifies cloud features on a sequence of images on the television, and the computer aids in tracking those features. The system is flexible and allows graphic overlays of the cloud drift measurements and measurements or contours of conventional surface and radiosonde data in addition to possessing enhancement capabilities.

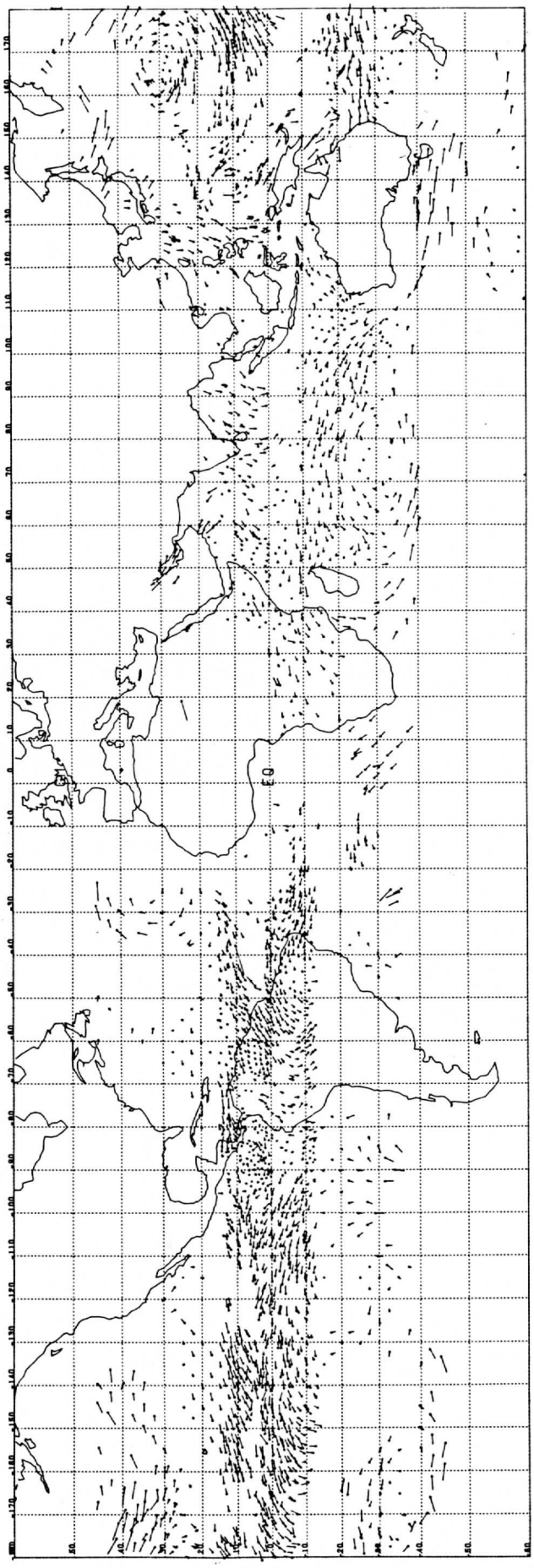

Fig. 4.5: Low level cloud tracked winds from 11 January 1979 from all the producers of cloud tracked winds.

Fig. 4.6: High level cloud tracked winds from 11 January 1979 from all the producers of cloud tracked winds.